# Sex-dependent interferon signaling drives female-biased vulnerability in Alzheimer's disease

Verónica López-López,[1] Gerard Iniesta,[1] Marcos Galán-Ganga,[2,3,4] Alejandro Expósito-Coca,[1] Aysha Bhojwani-Cabrera,[1] Marina Guillot-Fernández,[1] Albert Giralt,[2,3,4,5] José P. López-Atalaya[1]

[1]Instituto de Neurociencias, Consejo Superior de Investigaciones Científicas, Universidad Miguel Hernández, Alicante, Spain.

[2]Departament de Biomedicina, Facultat de Medicina, Institut de Neurociències, Universitat de Barcelona, Barcelona, Spain.

[3]Institut d'Investigacions Biomèdiques August Pi i Sunyer (IDIBAPS), Barcelona, Spain.

[4]Centro de Investigación Biomédica en Red sobre Enfermedades Neurodegenerativas (CIBERNED), Madrid, Spain.

[5]Production and Validation Centre of Advanced Therapies (Creatio), Faculty of Medicine and Health Science, University of Barcelona, Barcelona, Spain.

Correspondence: José P. López-Atalaya, Instituto de Neurociencias, Consejo Superior de Investigaciones Científicas, Universidad Miguel Hernández, Alicante, Spain. Phone: 34.965.23.3744. Email: jose.lopezatalaya@csic.es.

Conflict of interest: The authors have declared that no conflict of interest exists.

# Abstract

Alzheimer's disease (AD) disproportionately affects women, yet the neurobiological mechanisms underlying this sex bias remain poorly understood. Here, we identify a sex-dependent activation of type I interferon (IFN-I) signaling as a contributor to this disparity. Transcriptomic profiling of brain from AD patients revealed selective enrichment of IFN-I pathway in females. This immune signature was mirrored in the APP/PS1 mouse model of AD, where females exhibited more pronounced amyloid accumulation, neuroinflammation, and neurodegeneration. Acute IFN-I activation reproduced pathological features of AD, whereas chronic IFN-I elevation in APP/PS1 mice aggravated disease progression. In contrast, pharmacological targeting of IFN-I response by inhibiting the cGAS-STING pathway in APP/PS1 female mice reduced neuropathological burden, and preserved cognitive performance. Together, these findings identify interferon signaling as a modifiable and sex-linked driver of AD pathology. Our study uncovers a critical neuroimmune mechanism contributing to female-biased vulnerability and highlights interferon modulation as a promising therapeutic strategy in AD.



**Keywords:** Alzheimer's disease; Sex differences; Type I interferon; Interferon signaling; Neuroinflammation; cGAS–STING pathway; Learning and memory

# Introduction

Alzheimer's disease (AD) is a progressive and ultimately fatal neurodegenerative disorder and the most common cause of dementia worldwide (1–3). With an aging global population, the number of individuals affected by AD is projected to exceed 100 million by 2050, placing an enormous burden on healthcare systems and caregivers (1, 3–5). The neuropathological hallmarks of AD - extracellular amyloid-β plaques, intracellular tau neurofibrillary tangles, and chronic neuroinflammation - are accompanied by cognitive and behavioral impairments that progressively erode autonomy and quality of life (2, 3, 6). Despite decades of intense research, currently approved treatments provide only modest symptomatic relief, and no curative or disease-modifying therapies have yet been established (6–8).

A consistently reported yet underexplored feature of AD is its disproportionate impact on females. Females comprise nearly two-thirds of individuals diagnosed with AD (1, 3, 5), and lifetime risk estimates indicate that approximately 1 in 5 females, compared to 1 in 10 males, will develop the disease (1, 4). Although increased longevity contributes to this imbalance, it does not fully account for the observed differences (9–12). Clinical and neuroimaging studies have revealed that females with AD often exhibit faster cognitive decline, greater neuropathological burden, and more rapid progression from mild cognitive impairment to dementia than their male counterparts (9, 13–18). Biological sex thus acts as an independent modifier of AD risk and trajectory, shaping both susceptibility and disease course.

Despite its clinical significance, the mechanistic basis for sex-related differences in AD remains poorly defined. Historically, biological sex has been underrepresented or insufficiently analyzed in both clinical trials and experimental models (19–22). Many preclinical studies rely exclusively on male animals, or include both sexes without

71 stratified analysis, thereby missing potentially critical sex-dependent effects (20, 23–25).
72 This limitation not only undermines the translational relevance of preclinical findings but
73 also hinders the development of sex-informed therapeutic strategies.

74 Addressing this knowledge gap requires a targeted focus on molecular and cellular
75 pathways that are both central to AD pathogenesis and modulated by sex. In this regard,
76 the innate immune system - particularly neuroimmune signaling within glial networks -
77 has emerged as a key candidate. Genome-wide association studies (GWAS) have
78 identified numerous AD susceptibility loci involved in immune regulation, including
79 variants in *TREM2*, *CD33*, and *HLA* genes, among others (26–29). These discoveries have
80 expanded the conceptual framework of AD beyond classical amyloid and tau cascades,
81 implicating immune dysregulation and glial biology as core features of disease
82 pathogenesis (30–34).

83 In parallel, a growing body of research has shown that immune responses are
84 strongly shaped by biological sex. Females generally exhibit stronger baseline and
85 stimulus-induced immune responses, both peripherally and in the central nervous system
86 (35–39). While this amplified responsiveness may enhance pathogen clearance, it is also
87 linked to greater vulnerability to chronic inflammation and autoimmunity (35, 36, 38). In
88 the context of neurodegeneration, sex-biased immune traits may alter the threshold,
89 magnitude, or persistence of neuroinflammatory responses, potentially influencing
90 susceptibility to and progression of AD (14, 40–42).

91 Whether such immunological differences translate into distinct molecular
92 trajectories or pathological outcomes in AD remains an open question. Biological sex
93 may shape diverse cellular programs - including glial activation states (43–46), neuronal
94 vulnerability, and synaptic remodeling (47–50) - that collectively influence disease

95 dynamics. However, these hypotheses require systematic and mechanistic investigation.
96 Understanding how sex interacts with disease-relevant pathways is essential for
97 explaining observed clinical disparities and for identifying novel therapeutic targets that
98 reflect this dimension of disease biology.

99 In this study, we sought to investigate the molecular mechanisms underlying sex-
100 associated differences in AD vulnerability. We combined transcriptomic analysis of
101 *postmortem* human brain tissue with functional studies in established mouse models of
102 AD. By stratifying human samples by sex, age, and brain region, we identified a
103 pronounced activation of type I interferon (IFN-I) signaling in females. To explore the
104 causal role of sex-dependent IFN-I signaling in disease pathogenesis, we employed both
105 pharmacological and genetic manipulations *in vivo* and assessed the impact of modulating
106 IFN-I signaling on neuroinflammation, neuropathology, and cognitive performance. This
107 integrative approach establishes IFN-I signaling as a key contributor to sex-associated
108 differences in AD vulnerability and highlights its potential as a therapeutic target.
109

# Results

**Sex-Based Differences in Interferon Pathway Activation Are Associated with Increased Alzheimer's Risk and Prevalence in Women**

Epidemiological data from the Alzheimer's Facts and Figures 2024 report highlight a markedly increased lifetime risk of AD in women (51). At both 45 and 65 years of age, the estimated lifetime risk of developing AD is approximately 20% for women versus 10% for men (51–54). Among individuals aged 65 and older, women account for approximately 61% of all AD cases, while men account for 39% (51, 53, 55). These sex disparities in disease prevalence and risk are illustrated schematically (Fig. 1A).

While several clinical studies have reported faster disease progression and greater pathological burden in females (13, 14, 16, 17), the molecular mechanisms driving this increased vulnerability remain poorly understood. To address this, we leveraged RNA-sequencing data from the parahippocampal gyrus (PHG) of AD patients in the Mount Sinai Brain Bank (MSBB). To minimize potential confounding effects of age, we focused on individuals aged 60 to 90 years, yielding a final cohort of 34 females and 32 males (Fig. 1B and Supplementary Data Table 1).

Principal component analysis (PCA) confirmed robust sex-based separation and revealed one sample annotated as male that clustered instead with female samples (Extended Data Fig. 1A). Further analysis of sex chromosome gene expression - including *XIST* and *TSIX* from the X chromosome, and *UTY*, *RPS4Y1*, and *DDX3Y* from the Y chromosome - confirmed this misclassification (Extended Data Fig. 1B). This sample (marked in bold) was excluded from all subsequent analyses.

Differential gene expression analysis revealed a prominent female-biased transcriptional signature related to interferon signaling in AD patients, including genes

134 such as *GBP4*, *IFIT2*, *PSMB8*, *PSMB9*, *RTP4*, *B2M*, and *MX1* (Fig. 1C,D). Functional
135 enrichment analysis revealed that "Interferon Alpha Response" was the most significantly
136 enriched "hallmark" gene set (56) in females, followed by "Interferon Gamma Response"
137 and "p53 Pathway" (Fig. 1E). Gene Set Enrichment Analysis (GSEA) (57) further
138 confirmed strong and coordinated upregulation of the interferon alpha response pathway
139 in female AD samples (Fig. 1F).

140 To place these sex-stratified findings in the broader context of AD pathology, we
141 compared AD versus age-matched control samples without stratifying by sex (n = 108;
142 42 controls and 66 AD) (Supplementary Data Table 1). In this pooled analysis, functional
143 profiling identified "Epithelial Mesenchymal Transition" as the top enriched pathway,
144 followed by "Interferon Alpha Response" (Extended Data Fig. 1C), in addition to other
145 classical AD-associated pathways such as 'Cholesterol Homeostasis' (Supplementary
146 Data Table 1). However, stratifying by sex revealed a marked shift in the dominant
147 transcriptional programs: in males (n = 55; 23 controls and 32 AD), "Epithelial
148 Mesenchymal Transition" emerged as the principal upregulated pathway, whereas in
149 females (n = 53; 19 controls and 34 AD), "Interferon Alpha Response" became the
150 leading enriched pathway with, "Epithelial Mesenchymal Transition" ranking lower
151 (Extended Data Fig. 1D,E). This divergence underscores the critical influence of sex on
152 the molecular architecture of AD, revealing that the primary immune program engaged
153 by the disease differs fundamentally between males and females.

154 Next, we examined whether this transcriptional signature was also detectable
155 under non-pathological conditions. To this end, we analyzed transcriptomic data obtained
156 from the PHG of age-matched control individuals (n = 42; 19 females and 23 males)
157 (Supplementary Data Table 1). Functional analysis of sex-associated differentially

158 expressed genes revealed no significant enrichment of interferon-related pathways
159 (Extended Data Fig. 1F,G). A weak enrichment of the IFN-I response was detected in
160 GSEA (Extended Data Fig. 1H), suggesting that although females may exhibit slightly
161 higher baseline interferon tone, it is the presence of AD pathology that amplifies these
162 sex-dependent differences in a robust and functionally significant manner.

163 Together, these findings show that female AD patients exhibit a sustained
164 upregulation of IFN-I in the parahippocampal gyrus. This persistent immune activation
165 may contribute to the greater vulnerability and higher prevalence of AD observed in
166 women, highlighting sex-specific neuroimmune mechanisms as potential contributors to
167 disease susceptibility and progression.

168

169 **Sex-Specific Differences in Amyloid Pathology and Neurodegeneration in APP/PS1**
170 **Mice**

171 To evaluate whether the APPswe/PSEN1dE9 (APP/PS1) mouse model recapitulates the
172 sex-specific features of human AD, we analyzed male and female transgenic mice at 6
173 months of age (Fig. 2A). Immunohistochemical staining with the anti–amyloid-β (Aβ)
174 antibody 6E10 revealed significantly higher plaque burden in both the cortex and
175 hippocampus of female mice compared with males (Fig. 2B). Thioflavin T staining
176 confirmed these observations, showing more extensive fibrillar amyloid deposits in
177 females (Fig. 2C). Consistently, immunostaining with the OC antibody, which recognizes
178 β-sheet-rich Aβ conformations, revealed greater signal in female brains (Fig. 2D), further
179 validating increased pathological aggregation. Notably, plaque size was similar between
180 sexes (Extended Data Fig. 2A-C), suggesting that the sex difference primarily reflects
181 increased plaque number or density rather than altered morphology.

182 Building on these findings, we next examined other neuropathological features
183 associated with AD (58–62). Immunostaining for c-FOS, a marker of neuronal activity,
184 revealed reduced expression in the dentate gyrus of female mice (Fig. 2E), indicating
185 potential functional impairment. To assess inhibitory network integrity, we quantified
186 perineuronal nets (PNNs), specialized extracellular matrix structures that stabilize
187 synaptic connectivity (63). The proportion of parvalbumin-positive interneurons
188 surrounded by PNNs in the CA1 region was significantly lower in females, as visualized
189 by *Wisteria floribunda* agglutinin (WFA) staining (Fig. 2F,D). In parallel, we observed
190 increased axonal damage in the female hippocampus, as evidenced by elevated
191 phosphorylated neurofilament (pNF) staining (Fig. 2G). These converging
192 histopathological alterations suggest that female APP/PS1 mice experience more severe
193 neuronal dysfunction and structural disruption.

194 To determine whether these sex-specific differences extended to the
195 transcriptional level, we first characterized the global molecular profile of APP/PS1 mice
196 relative to wild-type controls. Bulk RNA-Seq of hippocampal tissue revealed pronounced
197 upregulation of transcripts related to the model's transgenes (*App*, *Prnp*) (64) alongside
198 microglial activation markers (*Clec7a*, *Trem2*, *Cst7, Itgax*) (65–67) (Extended Data Fig.
199 2E and Supplementary Data Table 3). Functional enrichment analysis indicated
200 significant activation of pathways including "Cholesterol Homeostasis", "Allograft
201 Rejection", and "Inflammatory Response" (Extended Data Fig. 2F), confirming that the
202 APP/PS1 model exhibits the expected immune–metabolic alterations associated with AD.

203 Building on this baseline characterization, we next examined whether the
204 transcriptional response to Aβ pathology differed between sexes. PCA revealed limited
205 separation between wild-type and APP/PS1 males, whereas APP/PS1 females diverged

206 markedly from wild-type females (Fig. 2H), indicating more extensive transcriptional
207 remodeling in females at this age (six month old). This suggests that female brains may
208 undergo a more profound molecular response to Aβ pathology, potentially contributing
209 to their heightened vulnerability.

210 These data indicate that female APP/PS1 mice exhibit greater amyloid deposition,
211 more pronounced neurodegeneration, and broader transcriptomic alterations than males.
212 Importantly, this model recapitulates the sex-specific vulnerability observed in human
213 Alzheimer's disease, making it a valuable platform for investigating the biological
214 mechanisms underlying these differences.
215

216 **Enhanced Neuropathology in Female APP/PS1 Mice Is Associated with Increased**
217 **Interferon Signaling**

218 To investigate potential molecular correlates of the more pronounced AD-like
219 histopathology observed in female APP/PS1 mice, we profiled gene expression of bulk
220 hippocampal tissue. In line with the differences found in AD patient´s (Fig. 1), differential
221 gene expression analysis revealed a significant upregulation of inflammatory genes in
222 females, including IFN-I-stimulated transcripts such as *Irf7*, *B2m*, *Psmb8*, *Psmb9*, *Ifit3*,
223 *Oas1a*, and *Rtp4* (Fig. 2I and Supplementary Data Table 3).

224 Given the observed transcriptional signature, we examined glial activation using
225 GFAP, a marker of astrogliosis and neuroinflammation (58, 68). Immunostaining
226 revealed higher densities of GFAP-positive astrocytes in the hippocampi of female mice
227 (Fig. 2J), with similar increases observed in the cortex (Extended Data Fig. 2G). While
228 this suggested enhanced neuroinflammation in females, GFAP is a broad marker and does
229 not reveal which specific inflammatory pathways are engaged. To further dissect the

230 molecular nature of immune activation, we performed functional analysis on significantly
231 differentially expressed genes using the “hallmark” gene sets collection (56). This
232 revealed a selective overrepresentation of interferon-related pathways in females,
233 including "Interferon Alpha Response” and "Interferon Gamma Response" (Fig. 2K),
234 indicating that the inflammatory profile in females is characterized by a pronounced
235 activation of antiviral IFN-I signaling. GSEA further supported these findings, revealing
236 a significant enrichment of the interferon alpha response gene set in APP/PS1 females
237 (Extended Data Fig. 2H).

238 To validate these transcriptomic findings at the protein level, we assessed the
239 expression of Ifitm3, a key effector of the interferon response. Immunohistochemistry
240 revealed significantly increased numbers of Ifitm3-positive cells in the hippocampus of
241 females compared with males (Fig. 2L), with similar results observed in the cortex
242 (Extended Data Fig. 2I).

243 Overall, our data indicate that the greater neurodegeneration and amyloid
244 pathology observed in female APP/PS1 mice is accompanied by a selectively heightened
245 interferon response, a feature that only emerged upon sex-stratified analysis, suggesting
246 interferon-related mechanisms as a potential driver of sex-specific vulnerability in AD.
247

248 **Interferon Induction by Viral-Mimetic Stimulation Is Sufficient to Elicit Alzheimer-**
249 **Like Histopathology**

250 Given the previously observed correlation between elevated interferon signaling and
251 worsened neuropathological features in female APP/PS1 mice, we next examined
252 whether interferon activation alone is sufficient to induce similar pathological changes.
253 To test this hyphotesis, we administered a single intraperitoneal dose of the viral mimetic

254 polyinosinic:polycytidylic acid [poly(I:C), 12 mg/kg] to 3-month-old wild-type C57BL/6
255 mice and analyzed brain tissue 24- and 72-hours post-injection (Fig. 3A).

256 First, we assessed the molecular response to poly(I:C) by profiling the
257 transcriptome of acutely isolated cortical microglia from adult mice 24 hours after
258 injection. PCA demonstrated clear separation between control and treated samples,
259 indicating a robust transcriptional shift (Extended Data Fig. 3A). Differential expression
260 analysis revealed strong upregulation of interferon-related genes, including *B2m*, *Psmb8*,
261 *Psmb9*, *Oas1a*, *Irf7*, *Gbp4*, *Rtp4*, *Stat2*, and *Ifit3* (Fig. 3B). Functional analysis confirmed
262 significant activation of pathways involved in interferon signaling and antiviral
263 responses, such as "Interferon Alpha Response", "Interferon Gamma Response", and
264 "Complement" (Fig. 3C, Extended Data Fig. 3B and Supplementary Data Table 4).

265 We next validated these transcriptional changes at the protein level by examining
266 Ifitm3 expression in relation to APP/PS1 pathology. Immunohistochemistry revealed
267 increased hippocampal Ifitm3 labeling in poly(I:C)-treated mice at 24- and 72-hours post-
268 injection, reaching levels similar to those observed in APP/PS1 mice (Fig. 3D). A similar
269 increase was noted in the cortex (Extended Data Fig. 3C), suggesting a shared interferon-
270 related molecular signature between acute poly(I:C) stimulation and chronic APP/PS1
271 pathology.

272 Given the marked interferon response, we assessed neuroinflammatory responses
273 by quantifying GFAP-positive astrocytes. Poly(I:C)-treated mice showed marked
274 astrogliosis in both the hippocampus (Fig. 3H) and cortex (Extended Data Fig. 2D),
275 mirroring the elevated GFAP levels observed in APP/PS1 mice. These findings indicate
276 that poly(I:C) is sufficient to elicit glial reactivity and inflammatory signaling in the brain.

277 To determine whether this interferon-driven inflammatory response could also
278 trigger structural and functional changes characteristic of Alzheimer's disease, we next
279 analyzed key histopathological features. At 72 hours post poly(I:C) treatment, reduced
280 cFOS immunostaining in the dentate gyrus suggested decreased neuronal activity,
281 mirroring the hypoactivity observed in APP/PS1 mice (Fig. 3E). We further evaluated
282 inhibitory circuit integrity by assessing PNNs. Poly(I:C) treatment reduced the proportion
283 of parvalbumin-positive interneurons surrounded by PNNs, with a comparable decrease
284 detected in APP/PS1 animals (Fig. 3F). This was accompanied by a global reduction in
285 WFA-labeled PNN structures (Extended Data Fig. 3E), indicating disruption of
286 extracellular matrix components critical for circuit stability. Finally, we assessed
287 neurodegeneration-related pathology by measuring pNF accumulation. Poly(I:C)
288 administration led to increased pNF immunoreactivity in the hippocampus, reaching
289 levels comparable to those observed in APP/PS1 mice (Fig. 3G), further supporting a link
290 between interferon signaling and neuronal injury.

291 Together, these findings reveal that acute activation of the interferon pathway via
292 viral-mimetic challenge is sufficient to elicit hallmark Alzheimer-related
293 histopathological alterations in healthy mice. These results establish a mechanistic link
294 between interferon responses, neuroinflammation, and neurodegeneration, supporting a
295 causative role for interferon activation in the pathogenesis of Alzheimer's-like features.
296

297 **Genetic Elevation of Interferon Signaling Enhances Alzheimer's-Related**
298 **Neuropathology**

299 We recently showed that *Rela* targeting in microglia leads to transcriptional
300 reprogramming towards an interferon-responsive state (Bhojwani-Cabrera et al.,
301 submitted manuscript). Taking advantage of this model and to assess the impact of

302 chronic interferon upregulation on AD progression, we generated a gain-of-function
303 model by crossing APP/PS1 mice with a tamoxifen-inducible, microglia-specific *Rela*
304 knockout line (Cx3cr1::CreERT2; Rela$^{fl/fl}$), hereafter referred to as AD hiIFN (Fig. 4A).
305 Mice were sacrificed at 6 months, allowing us to evaluate the impact of sustained
306 microglia-driven interferon upregulation during a critical window of Alzheimer's
307 pathology progression.

308 Efficient deletion of *Rela* in microglia was confirmed by qPCR performed on
309 fluorescence-activated cell sorted (FACS) microglia, showing significant reduction in
310 exons 1–3 and 6–7 expression, with a more pronounced decrease in exons 6–7 (Fig. 4B).
311 This genetic manipulation resulted in increased expression of interferon-related genes,
312 including *Irf7*, and *Ifitm3* (Fig. 4C).

313 Bulk RNA sequencing of hippocampal tissue revealed robust upregulation of
314 interferon-associated genes such as *B2m*, *Psmb9*, *Mx1, Irf7*, *Rtp4*, *Oas1a*, and *Ifit3* in AD
315 hiIFN mice compared to AD controls (Fig. 4D). PCA confirmed clear transcriptional
316 separation between genotypes, supporting a distinct molecular signature induced by
317 chronic interferon activation (Extended Data Fig. 4A). Gene ontology enrichment
318 analysis further highlighted significant overrepresentation of interferon and viral defense
319 pathways, including "Interferon Alpha Response" and "Interferon Gamma Response"
320 (Fig. 4E and Supplementary Data Table 5). Gene set enrichment analysis using the
321 "hallmark" gene set collection (56) confirmed enrichment of "Interferon Alpha
322 Response" pathway in AD hiIFN mice (Extended Data Fig. 4B).

323 To determine whether this transcriptional program was influenced by sex, we
324 compared interferon responses across male and female mice in the AD hiIFN model.
325 Analysis of the top 15 significantly upregulated interferon-stimulated genes AD hiIFN

326 revealed that both sexes reached comparable levels of interferon-related transcripts
327 (Extended Data Fig. 4C). Based on this observation, both male and female animals were
328 included in the analysis. Protein-level validation by Ifitm3 immunohistochemistry
329 confirmed elevated interferon activity in AD hiIFN mice, with increased labeling of
330 Ifitm3 in the hippocampus (Fig. 4F) and cortex (Extended Data Fig. 4D).

331 Having confirmed sustained interferon activation at both the transcriptomic and
332 protein levels we next assessed the consequences on key histopathological features.
333 GFAP immunostaining revealed markedly exacerbated astrogliosis in AD hiIFN mice,
334 with higher GFAP labeling in hippocampus (Fig. 4G) and, nearly to significance, in
335 cortex (Extended Data Fig. 4E). In the dentate gyrus, AD hiIFN mice showed a more
336 pronounced reduction of c-FOS expression than AD mice, suggesting further impairment
337 of neuronal activity (Fig. 4H). Structural alterations in inhibitory interneuron networks
338 were also apparent, with a decreased proportion of parvalbumin-positive interneurons
339 enwrapped by perineuronal nets in CA1 (Fig. 4I) and a global reduction in WFA-labeled
340 structures that approached significance (Extended Data Fig. 4F). Finally, axonal integrity
341 was impaired, shown by increased phosphorylated neurofilament staining in
342 hippocampus (Fig. 4J).

343 Interestingly, despite these exacerbated signs of neurodegeneration and gliosis,
344 amyloid plaque burden was reduced in AD hiIFN mice. Quantification with 6E10 (Fig.
345 4K), Thioflavin T (Fig. 4L), and OC antibodies (Fig. 4M) demonstrated lower plaque
346 density in both cortex and hippocampus, with largely comparable plaque size distribution
347 (Extended Data Fig. 4G-I).

348 These data identify IFN-I signaling as a disease-modifying mechanism in AD.
349 Chronic upregulation of the IFN-I axis exacerbates neuroinflammation and

350 neurodegeneration, uncoupling plaque load from neuronal damage and underscoring a
351 pathogenic role for interferon-driven processes in disease progression. These findings
352 highlight IFN-I signaling as a potential therapeutic target in AD.
353

354 **Reduction of Interferon Signaling Via STING Antagonism Ameliorates**
355 **Alzheimer's-Associated Histopathology**

356 Having demonstrated that elevated IFN-I signaling worsens AD pathology, we next
357 explored whether attenuating this pathway could yield neuroprotective effects. To address
358 this, APP/PS1 mice received intraperitoneal injections of C-176, a selective STING
359 antagonist that prevents Cys91 palmitoylation and thereby blocks downstream interferon
360 production (69), in alternate days from 3 to 6 months of age, matching the treatment
361 window used in the IFN-I gain-of-function model (Fig. 5A). These animals are hereafter
362 termed AD loIFN.

363 To validate the immunomodulatory effect of C-176, we first treated BV2
364 microglial cultures with poly(I:C) in the presence or absence of the compound. C-176
365 reduced expression of *Irf7* and *Ifitm3* while increasing levels of the anti-inflammatory
366 cytokine *Il-10*, supporting its efficacy in suppressing interferon signaling in vitro
367 (Extended Data Fig. 5A).

368 We next evaluated the transcriptional effects of targeting IFN-I signaling *in vivo*.
369 Given the sex differences observed in IFN-I activation across previous experiments, we
370 first assessed whether the transcriptional effects of C-176 were comparable between male
371 and female APP/PS1 mice. To this end, we assessed the top 15 significantly
372 downregulated interferon-stimulated genes in AD loIFN model. This analysis revealed a
373 robust suppression of interferon-related transcripts exclusively in C-176–treated females,
374 while gene expression in males remained largely unchanged (Extended Data Fig. 5B).

375 These findings suggest that the efficacy of interferon pathway inhibition is sex-dependent,
376 likely due to the already low interferon tone observed in untreated AD males. Based on
377 these results, transcriptomic analyses were focused on female mice, in whom C-176
378 produced a measurable molecular response.

379 Accordingly, differential gene expression analysis of hippocampal tissue from
380 treated versus untreated female APP/PS1 mice revealed significant downregulation of
381 key interferon-stimulated genes, including *Psmb8*, *Psmb9*, *Irf7*, *Irf9*, *Rtp4*, Oas1a, and
382 *Ifit3* (Fig. 5B). Functional analysis indicated a loss of interferon- and viral defense–
383 associated "hallmark" gene sets in the treated group, including "Interferon Gamma
384 Response" and "Interferon Alpha Response" (Fig. 5C and Supplementary Data Table 6).
385 GSEA further confirmed significant negative enrichment of the "Interferon Alpha
386 Response" pathway elicited by C-176 treatment (Extended Data Fig. 5C). Analysis of
387 male-specific datasets confirmed a minimal transcriptional response to C-176, with no
388 significant changes in interferon-related genes or pathways detected (Extended Data Fig.
389 5D,E).

390 Consistent with overall transcriptional changes, protein-level validation by
391 immunohistochemistry showed reduced numbers of Ifitm3-positive cells in the
392 hippocampus (Fig. 5D) and cortex (Extended Data Fig. 5F) of treated mice.

393 Critically, these transcriptional and protein-level effects coincided with
394 improvements in AD-related histopathological features. GFAP immunostaining revealed
395 a significant reduction in astrogliosis in hippocampus (Fig. 5E) with a similar trend
396 observed in cortex (Extended Data Fig. 5G). Neuronal activity, measured by c-FOS
397 expression in the dentate gyrus, was partially restored following C-176 treatment (Fig.
398 5F). The integrity of inhibitory circuits was also preserved, as reflected by an increased

399 proportion of parvalbumin-positive interneurons surrounded by PNNs (Fig. 5G) and a
400 concomitant rise in WFA-labeled PNN structures (Extended Data Fig. 5H). Axonal
401 integrity was likewise improved, as evidenced by a decrease in pNF staining in the
402 hippocampus (Fig. 5H).

403 Notably, despite these improvements in neuroinflammation and neuronal
404 preservation, amyloid pathology remained largely unchanged. Immunostaining with
405 6E10 revealed no significant differences in plaque burden in the hippocampus, with only
406 a modest, non-significant increase in the cortex (Fig. 5I). Thioflavin T staining confirmed
407 the absence of changes in plaque load across brain regions, whereas OC immunostaining
408 showed no significant difference in the hippocampus but a significant increase in plaque
409 burden in the cortex of treated mice (Fig.s 5J,K). Importantly, across all three markers,
410 plaque size showed a consistent trend toward reduction in treated animals (Extended Data
411 Fig. 5I–K), suggesting that IFN-I pathway inhibition may preferentially impact plaque
412 maturation and compaction rather than initial deposition.

413 In summary, pharmacological inhibition of IFN-I signaling via STING
414 antagonism mitigates key AD-related histopathological features, dampening
415 neuroinflammation and preserving neuronal integrity independently of plaque load and
416 pointing to IFN-I pathway suppression as a promising therapeutic approach for modifying
417 disease trajectory.

418

419 **Downregulation of Type I Interferon Signaling Preserves Cognitive Function in**
420 **Female APP/PS1 Mice**

421 Given our findings that heightened IFN-I signaling worsens Alzheimer pathology, while
422 its pharmacological inhibition alleviates key histological hallmarks, we next investigated
423 whether modulation of IFN-I activity also influences cognitive performance (Fig. 6A).

424 Specifically, we aimed to establish whether IFN-I signaling serves as a functional
425 mediator linking neuroimmune dysregulation to behavioral impairments in AD.

426 We first confirmed group-specific IFN-I activity by transcriptomic profiling of
427 hippocampal tissue. Comparison between female and male APP/PS1 mice revealed
428 selective upregulation of ISGs in females, including *Irf7*, *Irf9*, *Psbm8*, *Ifit3*, *Mx1, Rtp4*,
429 and *B2m*. These transcriptional changes were all attenuated by C-176 treatment in females
430 (Fig. 6B), indicating sex-dependent regulation of interferon signaling and its
431 pharmacological modulation.

432 Behavioral testing revealed domain-specific impairments in APP/PS1 mice, with
433 a clear sex bias emerging across tasks of increasing complexity. In the elevated plus maze
434 (EPM), no significant differences were observed between APP/PS1 males and their wild-
435 type counterparts. In contrast, APP/PS1 females spent significantly more time in the open
436 arms compared to wild-type females (Fig. 6C), consistent with altered anxiety-like
437 behavior. Similarly, Y-maze testing revealed impaired spontaneous alternation in females
438 - indicative of working memory deficits - while male APP/PS1 mice again performed
439 comparably to controls (Fig. 6D). However, in the novel object location test (NOLT),
440 which places higher demands on spatial memory, both male and female transgenic mice
441 failed to recognize the novel location (Fig. 6E). These findings parallel the sex-specific
442 pattern of IFN-I activation observed at the molecular level and support a functional link
443 between interferon dysregulation and cognitive decline.

444 To test this hypothesis directly, we evaluated whether suppression of IFN-I
445 signaling could ameliorate cognitive impairments in female APP/PS1 mice. Consistent
446 with transcriptomic evidence of ISG downregulation in the hippocampus (Fig. 6B), C-
447 176 treatment led to behavioral improvements across multiple domains. In the EPM,

448 treated mice spent significantly less time in the open arms compared to untreated
449 APP/PS1 females, resulting in anxiety-like behavior levels comparable to those observed
450 in control mice (Fig. 6F). In the Y-maze, C-176–treated females showed improved
451 spontaneous alternation, reaching performance levels comparable to wild-type controls
452 and indicative of restored working memory (Fig. 6G). Finally, in the more demanding
453 NOLT, treated mice successfully discriminated the novel location, in contrast to their
454 untreated counterparts (Fig. 6H), suggesting recovery of spatial memory function.

455 Notably, performance in the Open Field test was unaffected by genotype or
456 treatment, indicating no major alterations in locomotor activity or basal anxiety (Extended
457 Data Fig. 6A-E). Similarly, no significant differences were detected in the T-maze
458 (Extended Data Fig. 6B-F), contextual fear memory (Extended Data Fig. 6C-G) or cued
459 fear memory performance (Extended Data Fig. 6D-H), suggesting that not all cognitive
460 domains are equally influenced by interferon signaling.

461 Together, these data demonstrate that interferon signaling not only shapes
462 molecular and histopathological features of AD but also contributes to cognitive
463 dysfunction. Importantly, the ability of STING antagonism to reverse behavioral deficits
464 highlights IFN-I modulation as a promising avenue for therapeutic intervention aimed at
465 preserving cognitive function in AD.
466

467 # Discussion

468 Alzheimer's disease (AD) affects women disproportionately, both in prevalence and
469 progression rate (1, 3, 70–72). While demographic factors such as increased lifespan
470 contribute to this disparity, emerging evidence suggests that biological sex fundamentally
471 shapes the neurobiological response to AD pathology (12, 73). In this study, we show that
472 interferon signaling is selectively and robustly upregulated in the brains of female AD
473 patients and that this sex bias in immune activation corresponds with heightened
474 vulnerability to neurodegeneration in animal models. Through targeted manipulation of
475 the interferon axis *in vivo*, we establish a causal relationship between interferon activity
476 and hallmark features of AD pathology, including neuronal dysfunction, gliosis, and
477 cognitive decline.

478 Our transcriptomic analyses of the parahippocampal gyrus from AD patients
479 revealed significant enrichment of type I interferon response in females, along with
480 increased type II interferon. These pathways, well-characterized mediators of antiviral
481 immunity and inflammation, have been increasingly implicated in neurodegenerative
482 contexts (74–84). This observation builds on prior reports of sex differences in peripheral
483 immune responses (85–90) and extends them to the human brain, suggesting that female-
484 specific amplification of innate immunity may underlie increased AD susceptibility (91–
485 96).

486 To explore the functional relevance of these observations, we used the APP/PS1
487 mouse model of amyloidosis. Female transgenic mice exhibited more severe
488 neuropathology than males, including greater amyloid burden, increased glial activation,
489 and enhanced neuronal and axonal pathology. These histopathological findings were
490 mirrored by transcriptomic alterations, with female hippocampi displaying stronger

491 upregulation of interferon-stimulated genes and antiviral defense pathways. While sex
492 differences in AD models have been reported before (97–101), our work provides a
493 mechanistic framework linking female-biased IFN-I activation to downstream
494 neuropathological consequences.

495 Importantly, inducing IFN-I signaling in otherwise healthy wild-type mice - via
496 systemic administration of the viral mimetic poly(I:C) - was sufficient to reproduce
497 several AD-like features (102–104), including reduced neuronal activity (cFOS) (103,
498 104), degradation of perineuronal nets (PNNs) (105), astrogliosis (106), and axonal
499 damage (107). These findings align with prior demonstrations that chronic IFN-I impairs
500 neuronal function and plasticity; for instance, Baruch et al. showed that IFN-I drives
501 synaptic loss and cognitive decline in aging mice, while Blank et al. reported suppression
502 of hippocampal neurogenesis and long-term potentiation by IFN-I (108–112). Our
503 observation that both cFOS-positive neurons and PNNs decline following IFN-I
504 activation supports the idea that innate immune overactivation directly disrupts neuronal
505 circuits (80, 108, 113–115). These results extend the role of IFN-I in the CNS beyond
506 antiviral defense, positioning it as a key regulator of neural integrity.

507 The use of poly(I:C) to mimic viral activation also intersects with the long-
508 standing "infectious hypothesis" of AD, which posits that the disease may be driven, at
509 least in part, by host immune responses to chronic or latent infections (30, 34, 110).
510 Several studies have identified herpesvirus DNA in postmortem AD brains (116–119),
511 and recent transcriptomic analyses have revealed molecular signatures of past viral
512 exposure, including SARS CoV 2–related signals (120–123). Although causality remains
513 unresolved, our data show that even sterile mimetics of viral RNA can trigger key aspects

514 of AD pathology, reinforcing the notion that persistent immune stimulation can act as a
515 primary driver of neurodegeneration.

516 In this context, it is noteworthy that population-based studies have found
517 associations between vaccination against pathogens such as influenza and herpes zoster,
518 and a reduced incidence of dementia, including AD (124–128). Although mechanisms
519 remain speculative, one hypothesis is that vaccines reduce the frequency or severity of
520 viral reactivation and associated IFN-I bursts (114, 124, 129). Alternatively, they may
521 establish a more regulated immune tone less prone to maladaptive activation (74, 75,
522 127). Our data provides mechanistic support for these epidemiological associations,
523 suggesting that modulation of IFN-I activity may mediate the protective effects of
524 immunization.

525 To further assess the consequences of sustained IFN-I activation, we developed a
526 genetic gain-of-function model in which deletion of *Rela* in microglia reprogrammed
527 these cells toward an IFN-I-responsive phenotype (Bhojwani-Cabrera et al., submitted
528 manuscript). In that study, *Rela* knockout mice with heightened IFN-I pathway activation
529 exhibited cognitive impairment, consistent with previous reports linking increased
530 interferon signaling to cognitive decline (79, 83, 109, 112, 130, 131). When crossed with
531 APP/PS1 mice, this manipulation led to exacerbated neuroinflammation, axonal
532 pathology, and reduced neuronal activity. Interestingly, amyloid plaque burden was
533 reduced in these animals, indicating that IFN-I signaling can drive neurotoxicity through
534 mechanisms that are not strictly dependent on plaque accumulation (79, 80, 84). This
535 reflects a broader conceptual shift in the field - from viewing AD primarily as a disorder
536 of protein accumulation to recognizing the role of maladaptive immune responses (132–
537 134). Our findings parallel results from microglia-specific *C9orf72* knockout mice, which

538 also showed robust IFN-I signature accompanied by synaptic loss and reduced amyloid
539 deposition (135). However, the case of Ifitm3 - a key IFN-I effector - underscores the
540 complexity: although it enhances γ-secretase activity and amyloidogenesis (136), its
541 upregulation in *Rela* cKO brains coincided with fewer plaques, highlighting that its effect
542 may depend on the overall inflammatory context. Together, these observations suggest
543 that the neurotoxic impact of IFN-I responses may outweigh their influence on plaque
544 dynamics.

545 A key upstream trigger of IFN-I signaling in AD is activation of the cGAS–
546 STING pathway, which senses cytosolic DNA such as mitochondrial DNA released by
547 cellular stress - a process exacerbated near amyloid plaques (137–140). This pathway is
548 aberrantly activated in both AD models and human brain tissue, promoting IFN-I
549 responses and neuroinflammation (113, 141–144). Notably, our transcriptomic analyses
550 revealed increased p53 pathway activity in AD females compared to males, a relevant
551 finding given that p53 can amplify cGAS–STING signaling in response to DNA damage–
552 associated stress (145, 146). Consistent with these findings, we targeted STING using C-
553 176 in APP/PS1 mice. This treatment reduced IFN-I-stimulated gene expression,
554 dampened gliosis, preserved neuronal activity and axonal integrity, and improved
555 cognitive performance - particularly in females with higher baseline IFN-I levels.
556 Notably, these improvements occurred despite minimal changes in plaque burden,
557 reinforcing the idea that cGAS–STING–driven IFN-I responses contribute to
558 neurodegeneration independently of amyloid accumulation.

559 This dissociation between plaque deposition and clinical outcome mirrors
560 observations in "resilient" individuals - older adults with high amyloid load who remain
561 cognitively intact (147, 148). Postmortem analyses of such individuals often reveal low
562 glial activation and minimal inflammation (149, 150). Similarly, in C-176 treated mice,

563 IFN-I signaling was suppressed and cognitive function preserved despite persistent
564 plaques. These data strengthen the argument that the immune system - especially the IFN-
565 I axis - is a key determinant of whether amyloidosis remains subclinical or progresses to
566 overt neurodegeneration.

567 Although these results nominate the IFN-I axis as a compelling therapeutic target,
568 translation to the clinic demands scrutiny. C-176 has demonstrated efficacy in modulating
569 IFN-I signaling *in vivo* in murine models, yet its activity is confined to the murine STING
570 isoform, with no evidence supporting efficacy against the human variant (69, 151). By
571 contrast, compounds such as H-151 exhibit greater selectivity toward human STING and
572 represent more promising candidates for clinical development (69). Importantly,
573 preclinical data in murine models support the blood–brain barrier permeability and CNS
574 penetrance of these inhibitors, providing a promising pharmacokinetic basis for further
575 investigation (113, 152–154). Nonetheless, their pharmacokinetic properties in humans
576 remain to be characterized. Although IFN-I plays an essential role in host defense and
577 tumor surveillance, and systemic inhibition carries potential risks (115, 129, 155, 156),
578 several IFN-I-targeting agents - such as JAK inhibitors and anti IFNAR antibodies - are
579 already in clinical use for autoimmune disorders, providing a strong foundation for
580 repurposing (157–159). Patient stratification based on peripheral or cerebrospinal
581 biomarkers of IFN-I activity could further refine candidate selection and enhance
582 therapeutic precision.

583 These considerations underscore the need for precision medicine approaches that
584 account for interindividual variability in immune tone and response. Notably, our findings
585 emphasize the importance of sex as a biological variable in both disease progression and
586 therapeutic efficacy. Historically, females have been underrepresented in neuroscience

587 research, and many animal models fail to account for sex-based differences (11, 21, 22,
588 24). Here, the inclusion of both sexes revealed critical differences in pathology and a
589 female-specific therapeutic response to C-176 that would have been missed in a unisex
590 design. Moreover, the observation that epithelial–mesenchymal transition emerged as the
591 dominant pathway in males, whereas interferon alpha response predominated in females,
592 highlights fundamentally different disease-associated programs that may each warrant
593 tailored intervention. Future studies should address the potential pathogenic role of
594 epithelial–mesenchymal transition in male AD, as understanding these sex-specific
595 signatures will be essential for developing stratified therapeutic strategies in which sex
596 and immune phenotype guide clinical decision-making.

597 In conclusion, our study reveals that IFN-I signaling is selectively elevated in the
598 female AD brain and that this pathway actively contributes to neuronal and cognitive
599 dysfunction, independently of amyloid burden. By integrating human transcriptomics
600 with mechanistic animal models, we identify IFN-I as a central, sex-biased effector of
601 AD pathogenesis. These findings suggest that modulating IFN-I responses may offer
602 therapeutic benefit, particularly in patient populations characterized by heightened innate
603 immune activation. Future research should aim to identify biomarkers of IFN-I tone,
604 evaluate the safety of long-term IFN-I modulation, and determine whether early
605 intervention in IFN-I-dominant disease trajectories can prevent the transition from
606 asymptomatic amyloidosis to neurodegenerative decline.
607

608 # Methods

609 **Sex as a biological variable**

610 Both male and female mice were included in all experimental groups unless otherwise
611 stated, and sex was a central consideration in the study design. Experimental cohorts were
612 balanced by sex, and all transcriptomic, histological, and behavioral analyses were
613 stratified accordingly. This allowed for direct comparison of AD–related phenotypes and
614 immune signaling between male and female animals. Similarly, human transcriptomic
615 datasets from the The Mount Sinai Brain Bank (MSBB) study included 94 AD patients
616 (72 females and 32 males) and 34 age-matched healthy controls (17 females and 17
617 males), and differential expression analyses were performed to identify sex-specific
618 molecular signatures. Collectively, these approaches ensured that sex was rigorously
619 integrated as a biological variable throughout the study.

620

621 **Mice**

622 APP/PS1 (64) and Cx3cr1$^{CreER}$ (160) mice are available at public repositories
623 (RRID:MMRRC_034832-JAX and RRID:IMSR_JAX:021160, respectively). RelA$^{fl/fl}$
624 mice which harbor loxP sites flanking exons 5-8 of the *Rela* gene, have been previously
625 described (MGI:3775205) (161) and were kindly provided by Dr. Angel Barco (Instituto
626 de Neurociencias). Cx3cr1$^{CreER}$ mice were crossed with RelA$^{fl/fl}$ mice (161) resulting in
627 the line referred as Cx3cr1$^{CreER}$-Rela$^{fl/fl}$. These mice were crossed with APP/PS1 mice to
628 generate Cx3cr1$^{CreER}$-Rela$^{fl/fl}$-APP/PS1. In the experiments involving tamoxifen-induced
629 knockouts, we used tamoxifen-treated Rela$^{fl/fl}$-APP/PS1-littermates as controls. All
630 transgenic lines were maintained on a C57BL/6J genetic background.

631

632 **BV2 microglial cell line**

633 Mouse microglial BV2 cells were cultured in high-glucose Dulbecco's modified Eagle's
634 medium (DMEM) (Thermo Fisher Scientific, 41965047) supplemented with 10% heat-
635 inactivated fetal bovine serum (FBS) (Thermo Fisher Scientific, 10270106) and 1%
636 penicillin-streptomycin (Sigma-Aldrich, P4333). Cells were maintained at 37°C in a
637 humidified atmosphere with 5% $CO_2$ and plated at a density of $3 \times 10^5$ cells per well in
638 6-well plates for stimulation assays.
639
640 ***In vivo* animal treatments**
641 According to each experiment, animals were treated following ethical guides as described
642 previously. To induce Cre recombination in Cx3cr1$^{CreER}$ mice, tamoxifen (TMX) (Sigma-
643 Aldrich, T5648) was dissolved at 25 mg/mL in corn oil (Sigma-Aldrich, C8267) by
644 heating to 50°C for 1 hour under light-protected conditions. Three-month-old mice
645 received two intraperitoneal injections of tamoxifen (75 mg/kg) on alternate days. All
646 downstream experiments involving TMX were conducted at least one month after TMX
647 administration. Polyinosinic:polycytidylic acid high molecular weight (poly(I:C))
648 (Sigma-Aldrich, P1530-25MG) was prepared in sterile, endotoxin-free water and
649 administered intraperitoneally at a dose of 12 mg/kg. Mice were sacrificed at 24- or 72-
650 hours post-injection for transcriptomic and histological analyses. The STING inhibitor C-
651 176 (MedChemExpress, HY-112906) was prepared at 1.5 mg/mL in a corn oil:ethanol
652 (90:10) solution. Mice received intraperitoneal injections of 10 mg/kg on alternate days
653 from 3 to 6 months of age, corresponding to the window of APP/PS1 pathology
654 development.
655
656 **Immunohistochemistry and image analysis**

657 Mice were deeply anesthetized and transcardially perfused with PBS, followed by 4%
658 paraformaldehyde (PFA) (PFA, w/v, dissolved in 0.1 M phosphate buffer, pH 7.4). Brains
659 were post-fixed overnight and cryoprotected in 30% (w/v) sucrose for 48h. Coronal
660 sections (50 µm) were obtained using a cryotome and stored in antifreeze solution (30%
661 ethylene glycol, 30% glycerol, 30% distilled water, 10% PBS) at −20°C until processing.
662 Briefly, free-floating sections were washed 3 times in PBS (5 min each) and blocked in
663 5% Newborn calf serum (NCS) (Sigma-Aldrich, N4762) with 0.3% Triton X-100 (Sigma-
664 Aldrich, T8787), followed by overnight incubation at 4°C with primary antibodies. The
665 following primary antibodies were used: Ifitm3 (Proteintech, 11714-1-AP, 1:500), 6E10
666 (anti-β-Amyloid, 1–16) (BioLegend, 803001, 1:1000), c-FOS (Synaptic Systems,
667 226308, 1:1000), phosphorylated neurofilament (pNF) (Biolegend, SMI 31P, 1:500),
668 Parvalbumin (Synaptic Systems, 195004 1:1000), GFAP (Sigma-Aldrich, G3893, 1:500),
669 and OC (Sigma-Aldrich, AB2286, 1:5000). On the following day, slides were rinsed 3
670 times in PBS, incubated with fluorophore-conjugated secondary antibodies, and rinsed
671 again 3 times in PBS. The following secondary antibodies were used: Donkey anti-rat
672 IgG H+L Alexa Fluor 488 (Abcam, ab150153), Donkey anti-rabbit IgG H+L Alexa Fluor
673 647 (Abcam, ab150067), Donkey anti-mouse IgG H+L Alexa Fluor Plus 594 (Thermo
674 Fisher Scientific, A32744) and Donkey anti-guinea pig IgG H+L Alexa Fluor 647
675 (Abcam, 706-605-148), all at 1:500 dilution. Finally, tissue sections were counterstained
676 with DAPI (Thermo Fisher Scientific, A32733) and mounted onto glass slides using
677 Fluoromount- G (Sigma-Aldrich, T5941). For thioflavin T staining, after secondary
678 antibody staining, sections were incubated with 0.01% Thioflavin T (Sigma-Aldrich,
679 T3516) in water for 5 minutes, followed by 50% ethanol and PBS washes. For the
680 immunodetection of perineuronal nets (PNNs), after secondary antibody staining, slices
681 were incubated overnight at 4 °C with a solution containing biotinylated *Wisteria*

682 *floribunda* Lectin (WFA) (Vector Laboratories, B-1355-2, 1:300). On the following day,
683 sections were rinsed 3 times in PBS (5 min each) at RT, incubated with a solution of red
684 fluorescent streptavidin (Alexa Fluor™ 555 conjugate) (Thermo Fisher Scientifics,
685 S32356, 1:300) and 5% NCS in PBS for 1h at RT, and rinsed again 3 times in PBS.
686 Images were acquired using a Zeiss Axio Scan.Z1 slide scanner (20× objective).
687 Quantification was performed using Arivis Vision4D software, employing standardized
688 macros for image thresholding and segmentation. Regions of interest (ROIs) were
689 manually drawn around the dentate gyrus, CA1, cortex, or the entire hippocampus.
690 Quantification metrics included: total number of $cFOS^+$ nuclei in the dentate gyrus; total
691 number of $WFA^+$ objects and the percentage of $PV^+$ interneurons surrounded by PNNs in
692 the CA1 region; number and total area of $GFAP^+$ astrocytic objects; total $pNF^+$ area in
693 CA1; total number and area of $Ifitm3^+$ cells in cortex and hippocampus; amyloid plaque
694 density, number, and average size of Thioflavin $T^+$, $6E10^+$, and $OC^+$ amyloid deposits.
695

696 **FACS sorting of microglia**

697 Brains were collected and placed on ice in sterile phosphate-buffered saline (PBS). After
698 removal of the meninges, cortical hemispheres were mechanically dissociated in Dounce
699 buffer (15 mM HEPES, 0.5% glucose, HBSS 1x) using a tissue homogenizer (Fisher
700 Scientific, 10198611). Myelin was removed by centrifugation through a 25% isotonic
701 Percoll gradient at 800 x g for 15 minutes at 4°C. The resulting cell pellet was resuspended
702 in PBS, centrifuged, and processed for flow cytometry to isolate microglia as previously
703 described (Bhojwani-Cabrera et al., submitted manuscript). Briefly, Prior to antibody
704 staining, samples were blocked with Fc-block CD16/CD32 (Biolegend, 101320, 1:50) in
705 FACS Buffer sterile filtered (1% FCS, 2mM EDTA, 25mM HEPES in PBS) for 10 min
706 on ice and protected from light to block nonspecific binding. For cell surface staining,

707 cells were resuspended in the appropriate antibody cocktail and incubated for 30 min on
708 ice protected from light. Primary antibodies used were anti-mouse GFP (Aveslab, GFP-
709 1020, 1:500), anti-mouse Cd11b (BioLegend, 101235, 1:500), anti-mouse CD45
710 (BioLegend, 103106, 1:500). Samples were centrifuged and washed with FACS buffer.
711 Viability was assessed by staining with DAPI (1 µg/mL). Cells were sorted using a BD
712 FACS Aria III cell sorter (BD Bioscience). To sort the cells, a 85-micron nozzle with 4-
713 Way purity mode was used. The gating strategy involved selecting the cell population
714 based on forward scatter area (FSC-A) to discriminate cells by size, and side scatter area
715 (SSC-A) to separate them by granularity or internal complexity. Doublets were then
716 excluded by gating FSC-height (FSC-H) and FSC-A to isolate single cells. All final
717 analysis and data output were performed using FlowJo software (BD). For RNA-seq
718 experiments, microglia were isolated from the whole adult mouse cortex, yielding
719 200,000-300,000 cells. Sorted cells were collected directly into RLT buffer (Quiagen,
720 79216) for subsequent RNA extraction.
721
722 **Real-time quantitative PCR (RT-qPCR)**
723 To analyze gene expression in acutely FACS-isolated microglia from the adult mouse
724 hippocampus, RNA was extracted using the RNeasy Mini Kit (Qiagen, 74104) with on-
725 column DNase digestion (Thermo Fisher Scientific, 18047019). For BV2 cells, RNA was
726 isolated using TRIzol reagent (Thermo Fisher Scientific, A33251). For all samples, RNA
727 purity, integrity, and concentration were assessed by spectrophotometry (Nanodrop ND-
728 1000 spectrophotometer) and micro-capillary electrophoresis (2100 Bioanalyzer,
729 Agilent). Complementary DNA was synthesized using the RevertAid First Strand cDNA
730 Synthesis Kit (Thermo Fisher Scientific, EP0442) following the manufacturer's protocol,
731 and quantitative PCR was performed using EvaGreen Master Mix (Cultek, 755032) on a

732 QuantStudio 3 system (Applied Biosystems). Relative expression levels were analyzed
733 using the ΔΔCt method ((162), with Gapdh as the housekeeping gene for normalization.
734 Primer sequences used in RT–qPCR assays are listed in Supplementary Data Table 7.
735
736 **Human transcriptomic samples (MSBB Cohort)**
737 RNA-seq data from the parahippocampal gyrus (Brodmann area 36) were obtained from
738 the Mount Sinai Brain Bank (MSBB) via the AMP-AD Knowledge Portal (Synapse ID:
739 syn3159438; metadata: syn29855570; count data: syn27068754). We used processed raw
740 count matrices in which genes with fewer than 1 count per million (CPM) had already
741 been filtered out. For our analyses, we further subset the dataset to include only PHG
742 samples of AD cases aged 69 to 89 years at death. Resequenced samples were handled
743 by excluding unique sequencing batches; when biological replicates from the same
744 individual were available, those with higher RNA integrity (RIN and $RIN^2$ scores) were
745 preferentially retained. To reduce sex-related confounding effects, samples were
746 additionally filtered based on the expression of sex-linked genes, resulting in the removal
747 of one sample (see Extended Data Fig. 1). The final dataset included 33 female and 28
748 male AD cases. For additional analyses, samples were filtered using the same criteria,
749 selecting either control samples aged 69 to 89 years at death (17 females and 17 males)
750 or AD cases older than 69 years (72 females and 32 males).
751
752 **Mouse transcriptomic profiling by RNA-seq**
753 For the Alzheimer's disease-related samples **(**GSE304521**)**, total RNA was extracted
754 from hippocampi, rapidly dissected on ice using fine forceps. For the poly(I:C)-related
755 samples (GSE304362), total RNA was extracted from acutely FACS-isolated microglia
756 from the adult brain. For all samples, total RNA was extracted using the RNeasy Mini Kit

757 (Qiagen, 74104), including on-column DNase digestion (Thermo Fisher Scientific,
758 18047019). RNA quality was assessed by micro-capillary electrophoresis (Agilent
759 TapeStation, Agilent), and only samples with a RNA Integrity Number (RIN) ≥ 7 were
760 used for library construction. Libraries were amplified by PCR, purified, and size-selected
761 to enrich for fragments compatible with Illumina sequencing, followed by quality
762 assessment using fluorometry (Qubit fluorometer, Thermo Fisher Scientific) and micro-
763 capillary electrophoresis (Agilent TapeStation, Agilent). Libraries were prepared by
764 Novogene Europe (Cambridge, UK) using a strand-specific protocol with poly-A
765 selection and sequenced on an Illumina NovaSeq X Plus platform (PE150). For the
766 Alzheimer's disease-related samples (GSE304521), RNA-seq libraries were constructed
767 using Novogene NGS Stranded RNA Library Prep Set (PT044). Raw paired-end RNA-
768 seq reads in FASTQ format were processed by Novogene Europe (Cambridge, UK) using
769 their standard bioinformatics pipeline. Briefly, adapter sequences, reads containing poly-
770 N, and low-quality bases were removed using fastp (163). Quality metrics such as Q20,
771 Q30, and GC content were also calculated during this step. All downstream analyses were
772 based on the resulting high-quality clean reads. Clean reads were aligned to the mm39
773 mouse reference genome using HISAT2 (v2.2.1; (164)). The reference genome index was
774 built using HISAT2, and gene model annotations were used to enable splice-aware
775 alignment with improved accuracy. Library sizes of primary mapped reads were
776 consistently above 45 million fragments. Gene-level quantification was performed using
777 featureCounts (v2.0.6; (165)). The resulting count tables were used for downstream
778 differential expression analysis. For the poly(I:C)-related samples (GSE304362), RNA-
779 seq libraries were constructed using Novogene NGS RNA Library Prep Set (PT042). Raw
780 paired-end data were processed in-house following a custom analysis pipeline. Briefly,
781 raw paired-end RNA-seq reads in FASTQ format were first subjected to quality control

782 using FastQC (v0.11.9; https://www.bioinformatics.babraham.ac.uk/projects/fastqc/) to
783 assess base quality and sequence content. Adapter sequences and low-quality bases were
784 then removed using Trim Galore (v0.6.7; https://zenodo.org/records/7598955) in paired-
785 end mode. Post-trimming quality was re-evaluated with FastQC to confirm adapter
786 removal and improved read quality. High-quality reads were aligned to the GRCm38
787 mouse reference genome
788 using HISAT2 (v2.2.1; (166)) with the --dta option to facilitate downstream transcript
789 assembly. Library sizes of primary mapped reads were consistently above 50 million
790 fragments. Alignment output in SAM format was converted and sorted into BAM format
791 using SAMtools (v1.13; (167)), and subsequently indexed. For genome browser
792 visualization, BAM files were converted to TDF format using IGVTools (v2.5.3), aligned
793 to the mm10 genome build, and visualized in IGV (168). Gene-level quantification was
794 performed using HTSeq-count (v0.13.5) with parameters --stranded=no, --type=exon,
795 and --order=pos. Gene annotations were obtained from Ensembl release 102
796 (Mus_musculus.GRCm38.102.chr.gtf). The resulting count tables were used for
797 downstream differential expression analysis.
798
799 **Differential gene expression analysis**
800 Differential expression analyses were conducted in R version 4.5.0 (R Core Team, 2025)
801 using DESeq2 (v1.48.1; (169)), considering genes with adjusted P value < 0.05 as
802 significantly differentially expressed. Batch correction was applied when needed using
803 the ComBat_seq() function from the sva package (v3.56.0, (170)). To facilitate the
804 detection of batch effects, outliers, and major sources of variance, Principal Component
805 Analyses were performed on variance-stabilized data (VST for datasets with >30
806 samples) or regularized log-transformed data (rlog for datasets with <30 samples) using

807 the plotPCA() function from the DESeq2 package. The top 500 most variable genes were
808 used for dimensionality reduction. The first two principal components were visualized
809 with ggplot2 (v3.5.2, (171)), and sample labels were added using geom_text_repel() from
810 ggrepel (v0.9.6, (172))to improve readability. Heatmaps were generated on gene
811 expression counts rlog-transformed using pheatmap (v1.0.13, (173)), with hierarchical
812 clustering applied to genes and samples ordered by experimental design. Rows were
813 scaled using z-scores, and styling was harmonized with the overall plot design. Volcano
814 plots were generated using ggplot2, where the $-\log_{10}$ adjusted p-value was plotted against
815 the $\log_2$ fold change. Genes were color-coded by significance (padj < 0.05 or < 0.1) and
816 classified as upregulated, downregulated, or not significant. Key interferon-alpha–related
817 genes were labeled using ggrepel. Optional axis cutoffs were applied to reduce the impact
818 of extreme outliers on plot scaling.
819
820 **Functional enrichment analysis**
821 Functional enrichment analyses were performed on significantly differentially expressed
822 genes as input (padj < 0.05) using Enrichr (174) and the MSigDB "hallmark" 2020 gene
823 set collection (56). Gene Set Enrichment Analysis (GSEA) was performed to identify
824 coordinated shifts in predefined gene sets, using the GSEA_4.4.0 desktop application
825 (57), with the following parameters: 1,000 phenotype permutations, No_Collapse, and a
826 fixed permutation seed (149). Ranked gene lists (.rnk files) were created from DESeq2
827 output using tidyverse tools (v2.0.0, (175))without additional filtering. Enrichment was
828 tested against the MSigDB "hallmark" gene sets for both human (v2025.1.Hs) and mouse
829 (v2025.1.Mm) (56) GSEA plots were recreated in R using ggplot2, cowplot (v1.2.0,
830 (176)), and gridExtra (v2.3, (177)) to maintain stylistic consistency across visual outputs.
831

832 **Mouse behavioral testing**

833 All behavioral assays were conducted during the light phase under consistent illumination
834 (~20 lux) in a dedicated testing suite. Mice were acclimated to the testing room for at
835 least 30 minutes before each test. Behavior was recorded and analyzed using SMART 3.0
836 software (Panlab). We used adult mutant and control littermates of both sexes. For the
837 open field (OF) test, mice were placed in the center of a 40 × 40 × 40 cm arena and
838 allowed to explore freely for 15 minutes. Total distance traveled and time spent in the
839 center zone were recorded as measures of locomotor activity and anxiety-like behavior,
840 respectively. The *elevated plus maze* (EPM) consisted of two open and two closed arms
841 (30 × 5 cm), elevated 50 cm above the floor. Mice were placed in the center facing an
842 open arm and allowed to explore for 5 minutes. The percentage of time spent and number
843 of entries into open arms were calculated. To evaluate spatial working memory
844 spontaneous alternation was measured using the *Y-maze*. Briefly, the transparent
845 symmetrical Y-maze consisted of three arms (30 × 5 × 15 cm). Three objects of similar
846 size (∼20 cm3) were situated surrounding the maze at ∼15–20 cm outside the walls and
847 mice were allowed to freely explore the maze for 8 minutes. An alternation was defined
848 as sequential entry into all three arms (triad). Percent alternation = (Number of
849 alternations / [Total arm entries − 2]) × 100. To study short-term spatial memory, we used
850 the *T-maze*. The apparatus consisted of three arms, two of them situated at 180° from each
851 other and the third situated at 90° with respect to the other ones representing the stem arm
852 of the T. All three arms were 45 cm long. In the training trial, one arm was closed (novel
853 arm) and mice were placed in the stem arm of the T (home arm) and allowed to explore
854 this arm and the other available arm (familiar arm) for 10 min, after which they were
855 returned to the home cage. After an inter-trial interval of 1 h mice were placed in the stem
856 arm of the T-maze and allowed to freely explore all three arms for 5 min (testing phase).

857 The time in the new arm∗100/total time in the two arms at 180° was the parameter
858 evaluated. In the *novel object location* (NOLT) memory task, mice were habituated to a
859 40 × 40 cm arena for 15 minutes. Different distal visual cues were allocated in the walls
860 of the arena. On day 2, two identical objects were presented during a 10-minute
861 familiarization phase. After a 24-hour delay, one object was relocated to a novel position
862 (test phase), and mice were allowed to explore for 5 minutes. The discrimination index
863 was calculated as: (Time_novel − Time_familiar) / Total_exploration_time. Associative
864 memory was assessed using *fear conditioning paradigm*. A 25 x 25 x 25 cm black
865 chamber system was used (Panlab, Spain). On Day 1, animals were allowed to habituate
866 for 5 minutes. After habituation, a tone (90 dB) was presented for 30 seconds. During the
867 final 2 seconds of the tone, a 0.4 mA foot shock was administered for 1–2 seconds and
868 the mouse was allowed to remain 30 additional seconds in the chamber. This procedure
869 was repeated two times, and the mouse remained 2 additional minutes in the chamber
870 before removing it. On Day 2, the contextual memory test was conducted. The mouse
871 was placed in the chamber for 5 minutes, with no tone presented, and freezing behaviour
872 was recorded. Cued memory was assessed on day 3 in a novel context, consisting of a 5-
873 minute baseline followed by a 30-seconds tone presentation. Freezing was defined as the
874 absence of all movement except respiration for >1 second. Animals were tracked and
875 recorded with the Packwin V2.0.08 software (Panlab, Spain).
876
877 **Statistics**
878 Data are presented as mean ± standard error of the mean (SEM), unless otherwise
879 indicated. Statistical analyses were performed using GraphPad Prism (version 7) or R
880 (version 4.2 or later). For comparisons between two groups, unpaired two-tailed Student's
881 t tests were used. Comparisons involving more than two groups were analyzed using one-

882 way ANOVA followed by Bonferroni post hoc correction. For non-normally distributed
883 data, the Mann–Whitney U test was applied. Correlations were assessed using Pearson's
884 correlation coefficient. A *P* value less than 0.05 was considered statistically significant.
885 Specific statistical tests and sample sizes (n) for each experiment are reported in the figure
886 legends.
887
888 **Study approval**
889 The study was conducted in compliance with European Union Directive 2010/63/EU on
890 the protection of animals used for scientific purposes. All the protocols for animal
891 experimentation were approved by the Animal Welfare Committee at the Instituto de
892 Neurociencias, the CSIC Ethical Committee, and the Dirección General de Agricultura,
893 Ganadería y Pesca of Generalitat Valenciana. Mice were maintained under specific
894 pathogen-free (SPF) conditions at the Animal Facility of the Instituto de Neurociencias
895 (CSIC-UMH), on a 12 h light/12 h dark cycle (7:00 a.m. to 7:00 p.m.), at 20–24 °C and
896 40–60% controlled humidity, with *ad libitum* access to food and water.
897
898 **Data availability**
899 The transcriptomics data sets generated in this study can be accessed at the GEO public
900 repository using the accession number GSE304521 and GSE304362. In addition, human
901 RNA-seq data used in this study were obtained from the publicly available The Mount
902 Sinai Brain Bank (MSBB) study, hosted on the AD Knowledge Portal
903 (https://adknowledgeportal.org/). The dataset is accessible via Synapse
904 (https://www.synapse.org/): syn3159438; metadata: syn29855570; count data:
905 syn27068754). The results published here are in whole or in part based on data obtained
906 from the AD Knowledge Portal (https://adknowledgeportal.org/). These data were

907 generated from postmortem brain tissue collected through the Mount Sinai VA Medical
908 Center Brain Bank and were provided by Dr. Eric Schadt from Mount Sinai School of
909 Medicine. Processed data and code used for statistical analysis, gene expression
910 processing, and figure generation are available upon request from the corresponding
911 author.
912

## Author contributions

Conceptualization, V.L-L., and J.P.L-A.; methodology, V.L-L., M.G-G., G.I., A.E-C., A.B-C., A.G., and J.P.L-A.; investigation, V.L-L., M.G-G., and A.E-C.; data curation, V.L-L., M.G-G., G.I., and M.G-F.; formal analysis: V.L-L., M.G-G., and G.I.; writing – original draft, V.L-L., and J.L-A.; writing – review & editing, V.L-L., G.I., M.G-G., A.E-C., A.B-C., M.G-F., A.G., and J.L-A.; funding acquisition, J.P.L-A.; resources, J.P.L-A.; supervision, J.P.L-A. The order of authorship was determined by overall contributions and approved by the authors for the final manuscript.

## Acknowledgments

We thank Eduardo Soriano, Alberto Pascual, Jose V. Sánchez-Mut, and Berta L. Sánchez-Laorden for the critical reading of the manuscript. We are also grateful to members of the López-Atalaya laboratory for stimulating discussions throughout the course of this work. We thank the personnel of the Mouse Facility and the Microscopy and Omics Core Services at the Instituto de Neurociencias for their support and technical assistance. This study was supported by grant PID2021-129053OB-I00 funded by MCIU/AEI/10.13039/501100011033 and by ERDF, EU, and the Generalitat Valenciana, Conselleria d'Educació, Universitats i Ocupació (PROMETEO 2020/007) to J.P.L-A.; V.L-L. is the recipient of a 2021 neuroscience doctoral fellowship from the Fundación Tatiana Pérez de Guzmán el Bueno. G.I. holds a Formación de Personal Investigador (FPI) contract (CEX2021-001165-S-20-2), associated with "Severo Ochoa" grant CEX2021-001165-S from the MCIU/AEI/10.13039/501100011033. A.B-C. held a Formación de Personal Investigador (FPI) contract (PRE2019-090492), associated with grant RTI2018-102260-B-I00 awarded to J.P.L-A., and funded by MCIU/AEI/10.13039/501100011033 and by "ERDF A way of making Europe". M.G-F.

is the recipient of a Formación de Profesorado Universitario contract (FPU22/01375) funded by the Spanish Ministry of Science, Innovation and Universities (MICIU). The Institute of Neurosciences is a Severo Ochoa Center of Excellence (grant CEX2021-001165-S, funded by MCIU/AEI/10.13039/501100011033). This work was also funded by European Union NextGenerationEU/PRTR CNS2022 – 135391 ("Consolidación" program) and the Fundación Ramón Areces (CIVP21A7024) both to A.G. The project that gave rise to these results received the support of a fellowship from "la Caixa" Foundation (ID 100010434). The fellowship code is LCF/BQ/DR21/11880016 to M.G.-G.

# References


1. 2025 Alzheimer's disease facts and figures. *Alzheimer's & Dementia*. 2025;21(4). https://doi.org/10.1002/alz.70235.
2. Scheltens P, et al. Alzheimer's disease. *The Lancet*. 2021;397(10284):1577–1590.
3. Aguzzoli CS, et al. *World Alzheimer Report 2024 Global changes in attitudes to dementia Contributors: Survey translators*.
4. 2024 Alzheimer's disease facts and figures. *Alzheimer's and Dementia*. 2024;20(5):3708–3821.
5. Fang M, et al. Lifetime risk and projected burden of dementia. *Nat Med*. 2025;31(3):772–776.
6. Liu E, Zhang Y, Wang JZ. Updates in Alzheimer's disease: from basic research to diagnosis and therapies. *Transl Neurodegener*. 2024;13(1). https://doi.org/10.1186/s40035-024-00432-x.
7. Cummings JL, Osse AML, Kinney JW. Alzheimer's Disease: Novel Targets and Investigational Drugs for Disease Modification. *Drugs*. 2023;83(15):1387–1408.
8. Cummings J, et al. Alzheimer's disease drug development pipeline: 2023. *Alzheimer's and Dementia: Translational Research and Clinical Interventions*. 2023;9(2). https://doi.org/10.1002/trc2.12385.
9. Cui SS, Jiang QW, Chen S Di. Sex difference in biological change and mechanism of Alzheimer's disease: From macro- to micro-landscape. *Ageing Res Rev*. 2023;87. https://doi.org/10.1016/j.arr.2023.101918.
10. Aggarwal NT, Mielke MM. Sex Differences in Alzheimer's Disease. *Neurol Clin*. 2023;41(2):343–358.
11. Nebel RA, et al. Understanding the impact of sex and gender in Alzheimer's disease: A call to action. *Alzheimer's and Dementia*. 2018;14(9):1171–1183.
12. Lopez-Lee C, et al. Mechanisms of sex differences in Alzheimer's disease. *Neuron*. 2024;112(8):1208–1221.
13. Buckley RF, et al. Sex Differences in the Association of Global Amyloid and Regional Tau Deposition Measured by Positron Emission Tomography in Clinically Normal Older Adults. *JAMA Neurol*. 2019;76(5):542–551.
14. Rosenzweig N, et al. Sex-dependent APOE4 neutrophil–microglia interactions drive cognitive impairment in Alzheimer's disease. *Nat Med*. 2024;30(10):2990–3003.
15. Eikelboom WS, et al. Sex differences in neuropsychiatric symptoms in Alzheimer's disease dementia: a meta-analysis. *Alzheimers Res Ther*. 2022;14(1). https://doi.org/10.1186/s13195-022-00991-z.
16. Sohn D, et al. Sex Differences in Cognitive Decline in Subjects with High Likelihood of Mild Cognitive Impairment due to Alzheimer's disease. *Sci Rep*. 2018;8(1). https://doi.org/10.1038/s41598-018-25377-w.
17. Lin KA, et al. Marked gender differences in progression of mild cognitive impairment over 8 years. *Alzheimer's and Dementia: Translational Research and Clinical Interventions*. 2015;1(2):103–110.
18. Terstege DJ, Epp JR. Parvalbumin as a sex-specific target in Alzheimer's disease research – A mini-review. *Neurosci Biobehav Rev*. 2023;153. https://doi.org/10.1016/j.neubiorev.2023.105370.
19. Karp NA, Reavey N. Sex bias in preclinical research and an exploration of how to change the status quo. *Br J Pharmacol*. 2019;176(21):4107–4118.

20. Buckley RF, Gong J, Woodward M. A Call to Action to Address Sex Differences in Alzheimer Disease Clinical Trials. *JAMA Neurol*. 2023;80(8):769–770.
21. Beery AK, Zucker I. Sex bias in neuroscience and biomedical research. *Neurosci Biobehav Rev*. 2011;35(3):565–572.
22. Shansky RM. Are hormones a “female problem” for animal research? *Science (1979)*. 2019;364(6443):825–826.
23. Improving Bioscience Research Reporting: The ARRIVE Guidelines for Reporting Animal Research. *Vet Clin Pathol*. 2012;41(1):27–31.
24. Clayton JA, Collins FS. Policy: NIH to balance sex in cell and animal studies. *Nature*. 2014;509(7500):282–283.
25. Bale TL, Epperson CN. Sex as a Biological Variable: Who, What, When, Why, and How. *Neuropsychopharmacology*. 2017;42(2):386–396.
26. Bracher-Smith M, et al. Machine learning in Alzheimer’s disease genetics. *Nat Commun*. 2025;16(1):6726.
27. Jansen IE, et al. Genome-wide meta-analysis identifies new loci and functional pathways influencing Alzheimer’s disease risk. *Nat Genet*. 2019;51(3):404–413.
28. Bellenguez C, et al. New insights into the genetic etiology of Alzheimer’s disease and related dementias. *Nat Genet*. 2022;54(4):412–436.
29. Shade LMP, et al. GWAS of multiple neuropathology endophenotypes identifies new risk loci and provides insights into the genetic risk of dementia. *Nat Genet*. 2024;56(11):2407–2421.
30. Brown GC, Heneka MT. The endotoxin hypothesis of Alzheimer’s disease. *Mol Neurodegener*. 2024;19(1). https://doi.org/10.1186/s13024-024-00722-y.
31. Sarlus H, Heneka MT. Microglia in Alzheimer’s disease. *Journal of Clinical Investigation*. 2017;127(9):3240–3249.
32. Kinney JW, et al. Inflammation as a central mechanism in Alzheimer’s disease. *Alzheimer’s and Dementia: Translational Research and Clinical Interventions*. 2018;4:575–590.
33. Heneka MT, et al. Neuroinflammation in Alzheimer’s disease. *Lancet Neurol*. 2015;14(4):388–405.
34. Brutkiewicz RR, et al. What would it take to prove that a chronic infection is a causal agent in Alzheimer’s disease? *Trends Neurosci*. [published online ahead of print: 2025]. https://doi.org/10.1016/j.tins.2025.05.009.
35. Rubtsova K, Marrack P, Rubtsov A V. Sexual dimorphism in autoimmunity. *Journal of Clinical Investigation*. 2015;125(6):2187–2193.
36. Jacobsen H, Klein SL. Sex Differences in Immunity to Viral Infections. *Front Immunol*. 2021;12. https://doi.org/10.3389/fimmu.2021.720952.
37. Wilkinson NM, et al. Sex Differences in Immunity. *Annu Rev Immunol*. 2022;40:75–94.
38. Dunn SE, Perry WA, Klein SL. Mechanisms and consequences of sex differences in immune responses. *Nat Rev Nephrol*. 2024;20(1):37–55.
39. Klein SL, Flanagan KL. Sex differences in immune responses. *Nat Rev Immunol*. 2016;16(10):626–638.
40. Mangold CA, et al. Sexually divergent induction of microglial-associated neuroinflammation with hippocampal aging. *J Neuroinflammation*. 2017;14(1). https://doi.org/10.1186/s12974-017-0920-8.

41. Wen H, et al. Altered immune response is associated with sex difference in vulnerability to Alzheimer's disease in human prefrontal cortex. *Brain Pathology*. 2025;35(3). https://doi.org/10.1111/bpa.13318.
42. Buckley RF. Sex differences in Alzheimer's disease risk: Are immune responses the key? *Brain*. 2022;145(10):3341–3342.
43. Villa A, et al. Sex-Specific Features of Microglia from Adult Mice. *Cell Rep*. 2018;23(12):3501–3511.
44. Meadows SM, et al. Hippocampal astrocytes induce sex-dimorphic effects on memory. *Cell Rep*. 2024;43(6). https://doi.org/10.1016/j.celrep.2024.114278.
45. Rurak GM, et al. Sex differences in developmental patterns of neocortical astroglia: A mouse translatome database. *Cell Rep*. 2022;38(5). https://doi.org/10.1016/j.celrep.2022.110310.
46. Guneykaya D, et al. Transcriptional and Translational Differences of Microglia from Male and Female Brains. *Cell Rep*. 2018;24(10):2773-2783.e6.
47. Kim GS, Uddin M. Sex-specific and shared expression profiles of vulnerability and resilience to trauma in brain and blood. *Biol Sex Differ*. 2020;11(1). https://doi.org/10.1186/s13293-020-00288-6.
48. Kundakovic M, Tickerhoof M. Epigenetic mechanisms underlying sex differences in the brain and behavior. *Trends Neurosci*. 2024;47(1):18–35.
49. Mottron L, et al. Sex differences in brain plasticity: A new hypothesis for sex ratio bias in autism Understanding the links between sex/gender and autism Dr Meng-Chuan Lai. *Mol Autism*. 2015;6(1). https://doi.org/10.1186/s13229-015-0024-1.
50. Garrett JE, Wellman CL. Chronic stress effects on dendritic morphology in medial prefrontal cortex: sex differences and estrogen dependence. *Neuroscience*. 2009;162(1):195–207.
51. Aguzzoli CS, et al. *World Alzheimer Report 2024 Global changes in attitudes to dementia Contributors: Survey translators*.
52. Fang M, et al. Lifetime risk and projected burden of dementia. *Nat Med*. 2025;31(3):772–776.
53. 2024 Alzheimer's disease facts and figures. *Alzheimer's and Dementia*. 2024;20(5):3708–3821.
54. Moutinho S. Women twice as likely to develop Alzheimer's disease as men — but scientists do not know why. *Nat Med*. 2025;31(3):704–707.
55. 2025 Alzheimer's disease facts and figures. *Alzheimer's & Dementia*. 2025;21(4). https://doi.org/10.1002/alz.70235.
56. Liberzon A, et al. The Molecular Signatures Database Hallmark Gene Set Collection. *Cell Syst*. 2015;1(6):417–425.
57. Subramanian A, et al. *Gene set enrichment analysis: A knowledge-based approach for interpreting genome-wide expression profiles*. 2005.
58. Serrano-Pozo A, et al. Neuropathological alterations in Alzheimer disease. *Cold Spring Harb Perspect Med*. 2011;1(1). https://doi.org/10.1101/cshperspect.a006189.
59. Hendrickx A, et al. Epigenetic Regulations of Immediate Early Genes Expression Involved in Memory Formation by the Amyloid Precursor Protein of Alzheimer Disease. *PLoS One*. 2014;9(6):e99467-.
60. Crapser JD, et al. Microglia facilitate loss of perineuronal nets in the Alzheimer's disease brain. *EBioMedicine*. 2020;58. https://doi.org/10.1016/j.ebiom.2020.102919.
61. Dan L, Zhang Z. Alzheimer's disease: an axonal injury disease? *Front Aging Neurosci*. 2023;15. https://doi.org/10.3389/fnagi.2023.1264448.

1087 62. Corbett BF, et al. ΔFosB Regulates Gene Expression and Cognitive Dysfunction in
1088 a Mouse Model of Alzheimer's Disease. *Cell Rep*. 2017;20(2):344–355.
1089 63. Fawcett JW, Oohashi T, Pizzorusso T. The roles of perineuronal nets and the
1090 perinodal extracellular matrix in neuronal function. *Nat Rev Neurosci*. 2019;20(8):451–
1091 465.
1092 64. Jankowsky JL, et al. Mutant presenilins specifically elevate the levels of the 42
1093 residue β-amyloid peptide in vivo: evidence for augmentation of a 42-specific γ
1094 secretase. *Hum Mol Genet*. 2004;13(2):159–170.
1095 65. Keren-Shaul H, et al. A Unique Microglia Type Associated with Restricting
1096 Development of Alzheimer's Disease. *Cell*. 2017;169(7):1276-1290.e17.
1097 66. Sala Frigerio C, et al. The Major Risk Factors for Alzheimer's Disease: Age, Sex,
1098 and Genes Modulate the Microglia Response to Aβ Plaques. *Cell Rep*.
1099 2019;27(4):1293-1306.e6.
1100 67. Mathys H, et al. Temporal Tracking of Microglia Activation in Neurodegeneration at
1101 Single-Cell Resolution. *Cell Rep*. 2017;21(2):366–380.
1102 68. Pelkmans W, et al. Astrocyte biomarkers GFAP and YKL-40 mediate early
1103 Alzheimer's disease progression. *Alzheimer's and Dementia*. 2024;20(1):483–493.
1104 69. Haag SM, et al. Targeting STING with covalent small-molecule inhibitors. *Nature*.
1105 2018;559(7713):269–273.
1106 70. Subramaniapillai S, et al. Sex and gender differences in cognitive and brain
1107 reserve: Implications for Alzheimer's disease in women. *Front Neuroendocrinol*.
1108 2021;60. https://doi.org/10.1016/j.yfrne.2020.100879.
1109 71. Rosende-Roca M, et al. Exploring sex differences in Alzheimer's disease: a
1110 comprehensive analysis of a large patient cohort from a memory unit. *Alzheimer's*
1111 *Research and Therapy* . 2025;17(1). https://doi.org/10.1186/s13195-024-01656-9.
1112 72. Boccalini C, et al. Sex differences in the association of Alzheimer's disease
1113 biomarkers and cognition in a multicenter memory clinic study. *Alzheimer's Research*
1114 *and Therapy* . 2025;17(1). https://doi.org/10.1186/s13195-025-01684-z.
1115 73. Moutinho S. Women twice as likely to develop Alzheimer's disease as men — but
1116 scientists do not know why. *Nat Med*. 2025;31(3):704–707.
1117 74. Hammond TR, Marsh SE, Stevens B. Immune Signaling in Neurodegeneration.
1118 *Immunity*. 2019;50(4):955–974.
1119 75. Heppner FL, Ransohoff RM, Becher B. Immune attack: the role of inflammation in
1120 Alzheimer disease. *Nat Rev Neurosci*. 2015;16(6):358–372.
1121 76. Lopez-Atalaya JP, Bhojwani-Cabrera AM. Type I interferon signalling and
1122 interferon-responsive microglia in health and disease. *FEBS Journal*. [published online
1123 ahead of print: 2025]. https://doi.org/10.1111/febs.70126.
1124 77. Roy E, Cao W. Glial interference: impact of type I interferon in neurodegenerative
1125 diseases. *Mol Neurodegener*. 2022;17(1). https://doi.org/10.1186/s13024-022-00583-3.
1126 78. Wang Q, et al. Brain derived β-interferon is a potential player in Alzheimer's
1127 disease pathogenesis and cognitive impairment. *Alzheimer's Research and Therapy* .
1128 2024;16(1). https://doi.org/10.1186/s13195-024-01644-z.
1129 79. Roy ER, et al. Concerted type I interferon signaling in microglia and neural cells
1130 promotes memory impairment associated with amyloid β plaques. *Immunity*.
1131 2022;55(5):879-894.e6.
1132 80. Roy ER, et al. Type I interferon response drives neuroinflammation and synapse
1133 loss in Alzheimer disease. *Journal of Clinical Investigation*. 2020;130(4):1912–1930.

81. Tesseur I, et al. Deficiency in neuronal TGF-β signaling promotes neurodegeneration and Alzheimer's pathology. *Journal of Clinical Investigation*. 2006;116(11):3060–3069.
82. Kapoor M, Chinnathambi S. TGF-β1 signalling in Alzheimer's pathology and cytoskeletal reorganization: a specialized Tau perspective. *J Neuroinflammation*. 2023;20(1). https://doi.org/10.1186/s12974-023-02751-8.
83. Minter MR, et al. Deletion of the type-1 interferon receptor in APPSWE/PS1ΔE9 mice preserves cognitive function and alters glial phenotype. *Acta Neuropathol Commun*. 2016;4(1):72.
84. Sanchez-Garcia MA, et al. *Inactivation of the PHD3-FOXO3 axis blunts the type I interferon response in microglia and ameliorates Alzheimer's disease progression*. 2025.
85. Klein SL, Flanagan KL. Sex differences in immune responses. *Nat Rev Immunol*. 2016;16(10):626–638.
86. Rubtsova K, Marrack P, Rubtsov A V. Sexual dimorphism in autoimmunity. *Journal of Clinical Investigation*. 2015;125(6):2187–2193.
87. Ghosh S, Klein RS. Sex Drives Dimorphic Immune Responses to Viral Infections. *The Journal of Immunology*. 2017;198(5):1782–1790.
88. Giefing-Kröll C, et al. How sex and age affect immune responses, susceptibility to infections, and response to vaccination. *Aging Cell*. 2015;14(3):309–321.
89. Wilkinson NM, et al. Sex Differences in Immunity. *Annu Rev Immunol*. 2022;40:75–94.
90. Markle JG, Fish EN. SeXX matters in immunity. *Trends Immunol*. 2014;35(3):97–104.
91. Wen H, et al. Altered immune response is associated with sex difference in vulnerability to Alzheimer's disease in human prefrontal cortex. *Brain Pathology*. 2025;35(3). https://doi.org/10.1111/bpa.13318.
92. Buckley RF. Sex differences in Alzheimer's disease risk: Are immune responses the key? *Brain*. 2022;145(10):3341–3342.
93. Mangold CA, et al. Sexually divergent induction of microglial-associated neuroinflammation with hippocampal aging. *J Neuroinflammation*. 2017;14(1). https://doi.org/10.1186/s12974-017-0920-8.
94. Fyfe I. Immune responses influence sex differences in Alzheimer disease. *Nat Rev Neurol*. 2024;20(12):691.
95. Coales I, et al. Alzheimer's disease-related transcriptional sex differences in myeloid cells. *J Neuroinflammation*. 2022;19(1). https://doi.org/10.1186/s12974-022-02604-w.
96. Lopez-Lee C, et al. Tlr7 drives sex differences in age- and Alzheimer's disease–related demyelination. *Science (1979)*. 2024;386(6725). https://doi.org/10.1126/science.adk7844.
97. Stephen TL, et al. APOE genotype and sex affect microglial interactions with plaques in Alzheimer's disease mice. *Acta Neuropathol Commun*. 2019;7(1). https://doi.org/10.1186/s40478-019-0729-z.
98. Mifflin MA, et al. Sex differences in the IntelliCage and the Morris water maze in the APP/PS1 mouse model of amyloidosis. *Neurobiol Aging*. 2021;101:130–140.
99. Sala Frigerio C, et al. The Major Risk Factors for Alzheimer's Disease: Age, Sex, and Genes Modulate the Microglia Response to Aβ Plaques. *Cell Rep*. 2019;27(4):1293-1306.e6.

100. Yang J-T, et al. Sex Differences in Neuropathology and Cognitive Behavior in APP/PS1/tau Triple-Transgenic Mouse Model of Alzheimer's Disease. *Neurosci Bull*. 2018;34(5):736–746.
101. Jiao S-S, et al. Sex Dimorphism Profile of Alzheimer's Disease-Type Pathologies in an APP/PS1 Mouse Model. *Neurotox Res*. 2016;29(2):256–266.
102. Serrano-Pozo A, et al. Neuropathological alterations in Alzheimer disease. *Cold Spring Harb Perspect Med*. 2011;1(1). https://doi.org/10.1101/cshperspect.a006189.
103. Corbett BF, et al. ΔFosB Regulates Gene Expression and Cognitive Dysfunction in a Mouse Model of Alzheimer's Disease. *Cell Rep*. 2017;20(2):344–355.
104. Hendrickx A, et al. Epigenetic Regulations of Immediate Early Genes Expression Involved in Memory Formation by the Amyloid Precursor Protein of Alzheimer Disease. *PLoS One*. 2014;9(6):e99467-.
105. Crapser JD, et al. Microglia facilitate loss of perineuronal nets in the Alzheimer's disease brain. *EBioMedicine*. 2020;58. https://doi.org/10.1016/j.ebiom.2020.102919.
106. Pelkmans W, et al. Astrocyte biomarkers GFAP and YKL-40 mediate early Alzheimer's disease progression. *Alzheimer's and Dementia*. 2024;20(1):483–493.
107. Dan L, Zhang Z. Alzheimer's disease: an axonal injury disease? *Front Aging Neurosci*. 2023;15. https://doi.org/10.3389/fnagi.2023.1264448.
108. Deczkowska A, Baruch K, Schwartz M. Type I/II Interferon Balance in the Regulation of Brain Physiology and Pathology. *Trends Immunol*. 2016;37(3):181–192.
109. Baruch K, et al. Aging-induced type I interferon response at the choroid plexus negatively affects brain function. *Science (1979)*. 2014;346(6205):89–93.
110. Schwartz M, Deczkowska A. Neurological Disease as a Failure of Brain-Immune Crosstalk: The Multiple Faces of Neuroinflammation. *Trends Immunol*. 2016;37(10):668–679.
111. Mendoza-Fernández V, Andrew RD, Barajas-López C. Interferon-α inhibits long-term potentiation and unmasks a long-term depression in the rat hippocampus. *Brain Res*. 2000;885(1):14–24.
112. Blank T, et al. Brain Endothelial- and Epithelial-Specific Interferon Receptor Chain 1 Drives Virus-Induced Sickness Behavior and Cognitive Impairment. *Immunity*. 2016;44(4):901–912.
113. Gulen MF, et al. cGAS–STING drives ageing-related inflammation and neurodegeneration. *Nature*. 2023;620(7973):374–380.
114. Crow YJ. CNS disease associated with enhanced type I interferon signalling. *Lancet Neurol*. 2024;23(11):1158–1168.
115. Hu X, et al. Emerging role of STING signalling in CNS injury: inflammation, autophagy, necroptosis, ferroptosis and pyroptosis. *J Neuroinflammation*. 2022;19(1). https://doi.org/10.1186/s12974-022-02602-y.
116. Feng Y, et al. Human herpesvirus-associated transposable element activation in human aging brains with Alzheimer's disease. *Alzheimer's and Dementia*. 2025;21(2). https://doi.org/10.1002/alz.14595.
117. Huang SY, et al. Herpesvirus infections and Alzheimer's disease: a Mendelian randomization study. *Alzheimers Res Ther*. 2021;13(1). https://doi.org/10.1186/s13195-021-00905-5.
118. Eimer WA, et al. Alzheimer's Disease-Associated β-Amyloid Is Rapidly Seeded by Herpesviridae to Protect against Brain Infection. *Neuron*. 2018;99(1):56-63.e3.

119. Romanescu C, Schreiner TG, Mukovozov I. The Role of Human Herpesvirus 6 Infection in Alzheimer's Disease Pathogenicity—A Theoretical Mosaic. *J Clin Med*. 2022;11(11). https://doi.org/10.3390/jcm11113061.
120. Crivelli L, et al. Changes in cognitive functioning after COVID-19: A systematic review and meta-analysis. *Alzheimer's and Dementia*. 2022;18(5):1047–1066.
121. Bruno F, et al. Alzheimer's disease as a viral disease: Revisiting the infectious hypothesis. *Ageing Res Rev*. 2023;91. https://doi.org/10.1016/j.arr.2023.102068.
122. Levine KS, et al. Virus exposure and neurodegenerative disease risk across national biobanks. *Neuron*. 2023;111(7):1086-1093.e2.
123. Hu Y, et al. Infections among individuals with multiple sclerosis, Alzheimer's disease and Parkinson's disease. *Brain Commun*. 2023;5(2). https://doi.org/10.1093/braincomms/fcad065.
124. Ecarnot F, et al. Dementia, infections and vaccines: 30 years of controversy. *Aging Clin Exp Res*. 2023;35(6):1145–1160.
125. Pomirchy M, et al. Herpes Zoster Vaccination and Dementia Occurrence. *JAMA*. 2025;333(23):2083–2092.
126. Schnier C, et al. Reduced dementia incidence after varicella zoster vaccination in Wales 2013–2020. *Alzheimer's and Dementia: Translational Research and Clinical Interventions*. 2022;8(1). https://doi.org/10.1002/trc2.12293.
127. Lehrer S. *Vaccination Reduces Risk of Alzheimer's Disease, Parkinson's Disease, and Other Neurodegenerative Disorders*. 2022.
128. Eyting M, et al. A natural experiment on the effect of herpes zoster vaccination on dementia. *Nature*. 2025;641(8062):438–446.
129. McNab F, et al. Type I interferons in infectious disease. *Nat Rev Immunol*. 2015;15(2):87–103.
130. Hosseini S, et al. Type I Interferon Receptor Signaling in Astrocytes Regulates Hippocampal Synaptic Plasticity and Cognitive Function of the Healthy CNS. *Cell Rep*. 2020;31(7). https://doi.org/10.1016/j.celrep.2020.107666.
131. Deczkowska A, et al. Mef2C restrains microglial inflammatory response and is lost in brain ageing in an IFN-I-dependent manner. *Nat Commun*. 2017;8(1). https://doi.org/10.1038/s41467-017-00769-0.
132. Heneka MT, et al. Neuroinflammation in Alzheimer's disease. *Lancet Neurol*. 2015;14(4):388–405.
133. Sarlus H, Heneka MT. Microglia in Alzheimer's disease. *Journal of Clinical Investigation*. 2017;127(9):3240–3249.
134. Kinney JW, et al. Inflammation as a central mechanism in Alzheimer's disease. *Alzheimer's and Dementia: Translational Research and Clinical Interventions*. 2018;4:575–590.
135. Lall D, et al. C9orf72 deficiency promotes microglial-mediated synaptic loss in aging and amyloid accumulation. *Neuron*. 2021;109(14):2275-2291.e8.
136. Hur J-Y, et al. The innate immunity protein IFITM3 modulates γ-secretase in Alzheimer's disease. *Nature*. 2020;586(7831):735–740.
137. Jin M, et al. Tau activates microglia via the PQBP1-cGAS-STING pathway to promote brain inflammation. *Nat Commun*. 2021;12(1). https://doi.org/10.1038/s41467-021-26851-2.
138. Dhir A, et al. Mitochondrial double-stranded RNA triggers antiviral signalling in humans. *Nature*. 2018;560(7717):238–242.

139. Quan S, et al. The neuroimmune nexus: unraveling the role of the mtDNA-cGAS-STING signal pathway in Alzheimer's disease. *Molecular Neurodegeneration* . 2025;20(1). https://doi.org/10.1186/s13024-025-00815-2.
140. Udeochu JC, et al. Tau activation of microglial cGAS–IFN reduces MEF2C-mediated cognitive resilience. *Nat Neurosci*. 2023;26(5):737–750.
141. Huang Y, et al. Mechanism and therapeutic potential of targeting cGAS-STING signaling in neurological disorders. *Mol Neurodegener*. 2023;18(1). https://doi.org/10.1186/s13024-023-00672-x.
142. Xie X, et al. Activation of innate immune cGAS-STING pathway contributes to Alzheimer's pathogenesis in 5×FAD mice. *Nat Aging*. 2023;3(2):202–212.
143. Chung S, et al. Blockade of STING activation alleviates microglial dysfunction and a broad spectrum of Alzheimer's disease pathologies. *Exp Mol Med*. 2024;56(9):1936–1951.
144. Carling GK, et al. Alzheimer's disease-linked risk alleles elevate microglial cGAS-associated senescence and neurodegeneration in a tauopathy model. *Neuron*. 2024;112(23):3877-3896.e8.
145. Ghosh M, et al. Mutant p53 suppresses innate immune signaling to promote tumorigenesis. *Cancer Cell*. 2021;39(4):494-508.e5.
146. Ghosh M, et al. p53 engages the cGAS/STING cytosolic DNA sensing pathway for tumor suppression. *Mol Cell*. 2023;83(2):266-280.e6.
147. Rahimi J, Kovacs GG. Prevalence of mixed pathologies in the aging brain. *Alzheimers Res Ther*. 2014;6(9). https://doi.org/10.1186/s13195-014-0082-1.
148. Aizenstein HJ, et al. Frequent amyloid deposition without significant cognitive impairment among the elderly. *Arch Neurol*. 2008;65(11):1509–1517.
149. Barroeta-Espar I, et al. Distinct cytokine profiles in human brains resilient to Alzheimer's pathology. *Neurobiol Dis*. 2019;121:327–337.
150. Perez-Nievas BG, et al. Dissecting phenotypic traits linked to human resilience to Alzheimer's pathology. *Brain*. 2013;136(8):2510–2526.
151. Wang B, et al. The STING inhibitor C-176 attenuates MPTP-induced neuroinflammation and neurodegeneration in mouse parkinsonian models. *Int Immunopharmacol*. 2023;124:110827.
152. Kong L, et al. mtDNA-STING Axis Mediates Microglial Polarization via IRF3/NF-κB Signaling After Ischemic Stroke. *Front Immunol*. 2022;13. https://doi.org/10.3389/fimmu.2022.860977.
153. Zhang S, et al. Potential Therapeutic Value of the STING Inhibitors. *Molecules*. 2023;28(7). https://doi.org/10.3390/molecules28073127.
154. Decout A, et al. The cGAS–STING pathway as a therapeutic target in inflammatory diseases. *Nat Rev Immunol*. 2021;21(9):548–569.
155. Zitvogel L, et al. Type I interferons in anticancer immunity. *Nat Rev Immunol*. 2015;15(7):405–414.
156. Hopfner K-P, Hornung V. Molecular mechanisms and cellular functions of cGAS–STING signalling. *Nat Rev Mol Cell Biol*. 2020;21(9):501–521.
157. Schwartz DM, et al. JAK inhibition as a therapeutic strategy for immune and inflammatory diseases. *Nat Rev Drug Discov*. 2017;16(12):843–862.
158. Tanaka Y, Tummala R. Anifrolumab, a monoclonal antibody to the type I interferon receptor subunit 1, for the treatment of systemic lupus erythematosus: an overview from clinical trials. *Mod Rheumatol*. 2021;31(1):1–12.

159. Jones SA, Morand EF. Targeting Interferon Signalling in Systemic Lupus Erythematosus: Lessons Learned. *Drugs*. 2024;84(6):625–635.
160. Parkhurst CN, et al. Microglia promote learning-dependent synapse formation through brain-derived neurotrophic factor. *Cell*. 2013;155(7):1596–1609.
161. Steinbrecher KA, et al. Loss of Epithelial RelA Results in Deregulated Intestinal Proliferative/Apoptotic Homeostasis and Susceptibility to Inflammation. *The Journal of immunology (1950)*. 2008;180(4):2588–2599.
162. Livak KJ, Schmittgen TD. Analysis of Relative Gene Expression Data Using Real-Time Quantitative PCR and the 2−ΔΔCT Method. *Methods*. 2001;25(4):402–408.
163. Chen S, et al. Fastp: An ultra-fast all-in-one FASTQ preprocessor. *Bioinformatics*. Oxford University Press; 2018:i884–i890.
164. Kim D, et al. Graph-based genome alignment and genotyping with HISAT2 and HISAT-genotype. *Nat Biotechnol*. 2019;37(8):907–915.
165. Liao Y, Smyth GK, Shi W. FeatureCounts: An efficient general purpose program for assigning sequence reads to genomic features. *Bioinformatics*. 2014;30(7):923–930.
166. Kim D, et al. Graph-based genome alignment and genotyping with HISAT2 and HISAT-genotype. *Nat Biotechnol*. 2019;37(8):907–915.
167. Danecek P, et al. Twelve years of SAMtools and BCFtools. *Gigascience*. 2021;10(2). https://doi.org/10.1093/gigascience/giab008.
168. Thorvaldsdóttir H, Robinson JT, Mesirov JP. Integrative Genomics Viewer (IGV): High-performance genomics data visualization and exploration. *Brief Bioinform*. 2013;14(2):178–192.
169. Love MI, Huber W, Anders S. Moderated estimation of fold change and dispersion for RNA-seq data with DESeq2. *Genome Biol*. 2014;15(12). https://doi.org/10.1186/s13059-014-0550-8.
170. Zhang Y, Parmigiani G, Johnson WE. ComBat-seq: Batch effect adjustment for RNA-seq count data. *NAR Genom Bioinform*. 2020;2(3). https://doi.org/10.1093/nargab/lqaa078.
171. Wickham H. *ggplot2: Elegant Graphics for Data Analysis*. Cham: Springer International Publishing; 2016.
172. Slowikowski K. Automatically Position Non-Overlapping Text Labels with “ggplot2” [R package ggrepel version 0.9.6] [Internet]. *CRAN: Contributed Packages*. 2024. https://doi.org/10.32614/CRAN.PACKAGE.GGREPEL.
173. Kolde R. Pretty Heatmaps [R package pheatmap version 1.0.13] [Internet]. *CRAN: Contributed Packages*. 2025. https://doi.org/10.32614/CRAN.PACKAGE.PHEATMAP.
174. Kuleshov M V., et al. Enrichr: a comprehensive gene set enrichment analysis web server 2016 update. *Nucleic Acids Res*. 2016;44(1):W90–W97.
175. Wickham H, et al. Welcome to the Tidyverse. *J Open Source Softw*. 2019;4(43):1686.
176. Wilke CO. Streamlined Plot Theme and Plot Annotations for “ggplot2” [R package cowplot version 1.2.0] [Internet]. *CRAN: Contributed Packages*. 2025. https://doi.org/10.32614/CRAN.PACKAGE.COWPLOT.
177. Auguie B. Miscellaneous Functions for “Grid” Graphics [R package gridExtra version 2.3] [Internet]. *CRAN: Contributed Packages*. 2017. https://doi.org/10.32614/CRAN.PACKAGE.GRIDEXTRA.

# Figure legends

**Fig. 1. Enhanced interferon signaling correlates with female-biased Alzheimer's disease risk and prevalence.** (A) Diagram illustrating lifetime risk and prevalence of AD, with women showing higher risk (20% vs. 10%) and prevalence (61% vs. 39%) compared to men (Alzheimer's Facts and Figures 2024). (B) Cohort overview of RNA-sequencing data from the MSBB, comprising 34 female and 32 male AD patients (aged 60–90 years) for parahippocampal gyrus analysis. (C) Volcano plot of differential gene expression in female vs. male AD brains. Significantly upregulated genes (FDR < 0.05) are shown in orange, and genes with 0.05 ≤ FDR < 0.1 are shown in dark blue. Interferon alpha signaling genes are highlighted. (D) Heatmap showing elevated expression of the top differentially expressed (FDR < 0.1) interferon-related genes in female AD samples compared to male samples. (E) Functional enrichment analysis of significantly upregulated genes (FDR < 0.05) in female AD brains showing enrichment of interferon-alpha and interferon-gamma response pathways. (F) GSEA plot showing coordinated upregulation of the interferon alpha response pathway in female AD brains.

**Fig. 2. Sex-specific amyloid pathology and interferon signaling in APP/PS1 mice.** (A) Schematic diagram of the APPswe/PSEN1dE9 (APP/PS1) mouse model, with experiments conducted at 6 months of age. (B) IHC with 6E10 antibody showing Aβ plaque density in cortex (CTX, $^{**}P < 0.01$) and hippocampus (HC, $^{*}P < 0.05$) of male and female mice, with higher burden in females (quantified graphs, Mann-Whitney test). (C) Thioflavin T staining of fibrillar Aβ deposits in CTX ($^{**}P < 0.01$) and HC ($^{*}P < 0.05$), with increased density in females (quantified graphs, Mann-Whitney test). (D) OC antibody staining of β-sheet-rich Aβ conformations in CTX and HC, showing greater signal in females (quantified graphs, $^{*}P < 0.05$, Mann-Whitney test). (E) c-FOS immunostaining in dentate gyrus, indicating reduced neuronal activity in female mice (quantified graphs, $^{*}P < 0.05$, Mann-Whitney test). (F) PNNs stained with PV/WFA in CA1, with lower proportion of PV+ interneurons in females (quantified graphs, $^{**}P < 0.01$, Mann-Whitney test). (G) pNF staining for axonal damage in HC, with higher levels in females (quantified graphs, $^{*}P < 0.05$, Mann-Whitney test). (H) PCA of hippocampal RNA-seq data, showing greater transcriptomic divergence in female APP/PS1 mice. (I) Volcano plot of differentially expressed genes in female vs. male hippocampus, highlighting upregulated interferon alpha genes (e.g., *Irf7*, *B2m*). (L) GFAP immunohistochemistry in HC, with increased cell density in females (quantified graphs, $^{*}P < 0.05$, Mann-Whitney test). (K) Functional enrichment analysis indicating an enrichment in the interferon alpha and gamma response pathways in female APP/PS1 mice. (L) Ifitm3 immunohistochemistry in HC, with increased labeling in females (quantified graphs, $^{*}P < 0.05$, Mann-Whitney test). Data from 6-month-old APP/PS1 mice. IHC: n = 12 (6 females, 6 males). RNA-seq: n = 16 (8 females, 8 males). Data represent mean ± SEM.

**Fig. 3. Poly(I:C)-induced interferon signaling elicits Alzheimer-like pathology**. (A) Schematic of experimental design with intraperitoneal poly(I:C) administration (12 mg/kg) to 3-month-old wild-type C57BL/6 mice, analyzed at 24 and 72 hours, and compared to APP/PS1 mice using microglia RNA-sequencing and immunohistochemistry (IHC). (B) Volcano plot of differentially expressed genes in hippocampus 24 hours post-poly(I:C), highlighting upregulated interferon alpha-related genes (e.g., *Irf7*, *Stat2*, *Ifit3*). (C) Functional enrichment analysis showing activation of interferon alpha/gamma pathways in poly(I:C)-treated mice. (D) Ifitm3

immunohistochemistry in hippocampus, with increased labeling in poly(I:C) 24h (*$P$ < 0.05), 72h (**$P$ < 0.01), and APP/PS1 (**$P$ < 0.01) compared to controls (quantified graphs, one-way ANOVA with Bonferroni post hoc test). (E) GFAP immunohistochemistry in hippocampus, with increased labeling in poly(I:C) 24h (**$P$ < 0.01), 72h (****$P$ < 0.0001), and APP/PS1 (****$P$ < 0.0001) compared to controls (quantified graphs, one-way ANOVA with Bonferroni post hoc test). (F) c-FOS immunostaining in dentate gyrus, showing reduced neuronal activity in poly(I:C) 72h (**$P$ < 0.01), and APP/PS1(****$P$ < 0.0001) vs. controls (quantified graphs, one-way ANOVA with Bonferroni post hoc test). (G) PNNs stained with PV/WFA in CA1, with lower proportion of PV+ interneurons in poly(I:C) 72h (****$P$ < 0.0001), and APP/PS1 (*$P$ < 0.05) vs. controls (quantified graphs, one-way ANOVA with Bonferroni post hoc test). (H) pNF staining for axonal damage in hippocampus, with higher levels in poly(I:C) 72h (*$P$ < 0.05), and APP/PS1 (**$P$ < 0.01) vs. controls (quantified graphs, one-way ANOVA with Bonferroni post hoc test). Data from wild-type and APP/PS1 mice. IHC: n = 8 (control), 4 (Poly(I:C) 24h), 4 (Poly(I:C) 72h), and 6 (APP/PS1). Poly(I:C) groups included only males; other groups were sex-balanced (3 females, 3 males for APP/PS1; 4 females, 4 males for controls). RNA-seq: n = 4 (control), 3 (Poly(I:C) 24h). Data represent mean ± SEM.

**Fig. 4. Enhanced interferon signaling exacerbates Alzheimer's pathology.** (A) Schematic of APP/PS1 (AD) crossed with microglia-specific *Rela* knockout (AD hiIFN) model, with tamoxifen induction at 3 months and analysis at 6 months using qPCR, bulk-RNAseq and immunohistochemistry (IHC). (B) qPCR showing *Rela* deletion efficiency in microglia (exons 1-3 and 6-7) in AD hiIFN vs. AD (quantified graphs, **$P$ < 0.01, Mann-Whitney test). (C) Microglia qPCR showing increased expression of interferon-related genes (e.g., *Irf7, Ifitm3)* in AD hiIFN hippocampus (quantified graphs, **$P$ < 0.01, Mann-Whitney test). (D) Volcano plot of differentially expressed genes in AD hiIFN vs. APP/PS1 controls, highlighting upregulated interferon alpha genes. (E) Functional enrichment analysis showing interferon alpha/gamma response pathways in AD hiIFN. (F) Ifitm3 immunohistochemistry in hippocampus, with higher labeling in AD hiIFN vs. AD (quantified graphs, **$P$ < 0.01, Mann-Whitney test). (G) GFAP immunohistochemistry for astrogliosis in hippocampus, showing increased density in AD hiIFN vs AD (quantified graphs, **$P$ < 0.01, Mann-Whitney test). (H) c-FOS immunohistochemistry in dentate gyrus, indicating reduced neuronal activity in AD hiIFN vs. AD (quantified graphs, *$P$ < 0.05, Mann-Whitney test). (I) PNNs stained with PV/WFA in CA1, with lower proportion of PV+ interneurons in AD hiIFN vs. AD (quantified graphs, *$P$ < 0.05, Mann-Whitney test). (J) pNF staining for axonal damage in hippocampus, with higher levels in AD hiIFN vs. AD (quantified graphs, **$P$ < 0.01, Mann-Whitney test). (K) 6E10 immunohistochemistry for Aβ plaque density, showing reduced burden in AD hiIFN vs. AD both in cortex (CTX) and hippocampus (HC) (quantified graphs, *$P$ < 0.05, Mann-Whitney test). (L) Thioflavin T staining for fibrillar Aβ deposits, with lower density in AD hiIFN vs. AD in CTX (*$P$ < 0.05) and HC (**$P$ < 0.01), (quantified graphs, Mann-Whitney test). (M) OC staining for β-sheet-rich Aβ conformations, with reduced signal in AD hiIFN vs. AD in CTX and HC, (quantified graphs, **$P$ < 0.01, Mann-Whitney test). Data from 6-month-old AD hiIFN and APP/PS1 mice. IHC: n = 6 per group (3 females, 3 males). RNA-seq: n = 8 per group (4 females, 4 males). Data represent mean ± SEM.

**Fig. 5. STING inhibition alleviates Alzheimer's pathology in APP/PS1 mice.** (A) Schematic of experimental design with STING inhibitor C-176 (10 mg/kg) administration

to 3-month-old APP/PS1 mice (AD loIFN), treated until 6 months, analyzed using bulk RNA-seq and immunohistochemistry (IHC). (B) Volcano plot of differentially expressed genes in hippocampus of treated vs untreated females, highlighting downregulated interferon alpha genes. (C) Functional enrichment analysis showing reduced interferon alpha/gamma response pathways in untreated vs. treated females. (D) Ifitm3 immunohistochemistry in hippocampus, with lower labeling in treated AD loIFN vs. untreated AD mice (quantified graphs, $*P < 0.05$, Mann-Whitney test). (E) GFAP immunohistochemistry for astrogliosis in hippocampus, showing decreased density in treated vs. untreated mice (quantified graphs, $*P < 0.05$, Mann-Whitney test). (F) c-FOS immunohistochemistry in dentate gyrus, indicating increased neuronal activity in treated vs. untreated mice (quantified graphs, $***P < 0.001$, Mann-Whitney test). (G) PNNs stained with PV/WFA in CA1, with higher proportion of PV+ interneurons in treated AD loIFN vs. untreated AD mice (quantified graphs, $**P < 0.01$, Mann-Whitney test). (H) pNF staining for axonal damage in hippocampus, with lower levels in treated vs. untreated mice (quantified graphs, $**P < 0.01$, Mann-Whitney test). (I) 6E10 immunohistochemistry for Aβ plaque density, showing non-significant changes in AD loiIFN vs. AD both in cortex (CTX) and hippocampus (HC) (quantified graphs, ns, $P > 0.05$, Mann-Whitney test). (J) Thioflavin T staining for fibrillar Aβ deposits, with no changes in treated vs. untreated mice both in CTX and HC quantified graphs, ns, $P > 0.05$, Mann-Whitney test). (K) OC staining for β-sheet-rich Aβ conformations, with increased signal in AD loIFN vs. AD in CTX ($*P < 0.05$) and non-significant changes in HC (ns, $P > 0.05$) (quantified graphs, Mann-Whitney test). Data from 6-month-old AD loIFN and APP/PS1 mice. IHC: n = 6 per group (3 females, 3 males). RNA-seq: n = 8 AD (females), 4 AD loIFN (females). Data represent mean ± SEM.

**Fig. 6. Downregulation of Interferon Signaling Preserves Cognitive Performance in Female APP/PS1 Mice**. (A) Schematic of experimental design for cognitive testing in male and female APP/PS1 mice (AD) and female APP/PS1 mice treated with C-176 (AD loIFN) from 3 to 6 months. (B) Heatmap of the top 15 upregulated interferon-alpha–related genes in hippocampal tissue from female AD mice, showing elevated expression compared to both male AD mice and C-176–treated female AD mice. (C) Elevated Plus Maze (EPM) results, showing increased time in open arms in female AD mice compared to WT females ($****P < 0.0001$), with no differences in males (ns, $P > 0.05$) (quantified graphs, $***P < 0.001$, one-way ANOVA with Bonferroni post hoc test). (D) Y-Maze spontaneous alternation, revealing reduced alternation in female AD mice compared to WT ($*P < 0.05$), with no differences in males (ns, $P > 0.05$) (quantified graphs, one-way ANOVA with Bonferroni post hoc test). (E) Novel Object Location Test (NOLT) results, indicating impaired spatial memory in both male and female AD mice compared to WT (quantified graphs, $***P < 0.001$, $****P < 0.0001$, ns $P > 0.05$, one-way ANOVA with Bonferroni post hoc test). (F) EPM in AD C-176-treated females, indicating normalized time in open arms compared to treated WT females (ns, $P > 0.05$) and demonstrating cognitive improve compared to untreated AD females ($*P < 0.05$) (quantified graphs, $***P < 0.001$, one-way ANOVA with Bonferroni post hoc test). (G) Y-maze in AD C-176-treated females, indicating normalized time in open arms compared to treated WT females (ns, $P > 0.05$) (quantified graphs, $*P < 0.05$, one-way ANOVA with Bonferroni post hoc test). (H) NOLT in C-176-treated female AD mice (AD loIFN), showing restored discrimination of novel object location compared to untreated AD females (quantified graphs, $***P < 0.001$, ns $P > 0.05$, one-way ANOVA with Bonferroni post hoc test). Data from 6-month-old WT, AD, and AD loIFN mice. n = 5 (male WT), 6 (male AD), 5

1518 (female WT), 5 (female AD), 5 (female WT + vehicle), 5 (female WT + C-176), 5 (female
1519 AD + vehicle), and 5 (female AD + C-176). Data represent mean ± SEM.

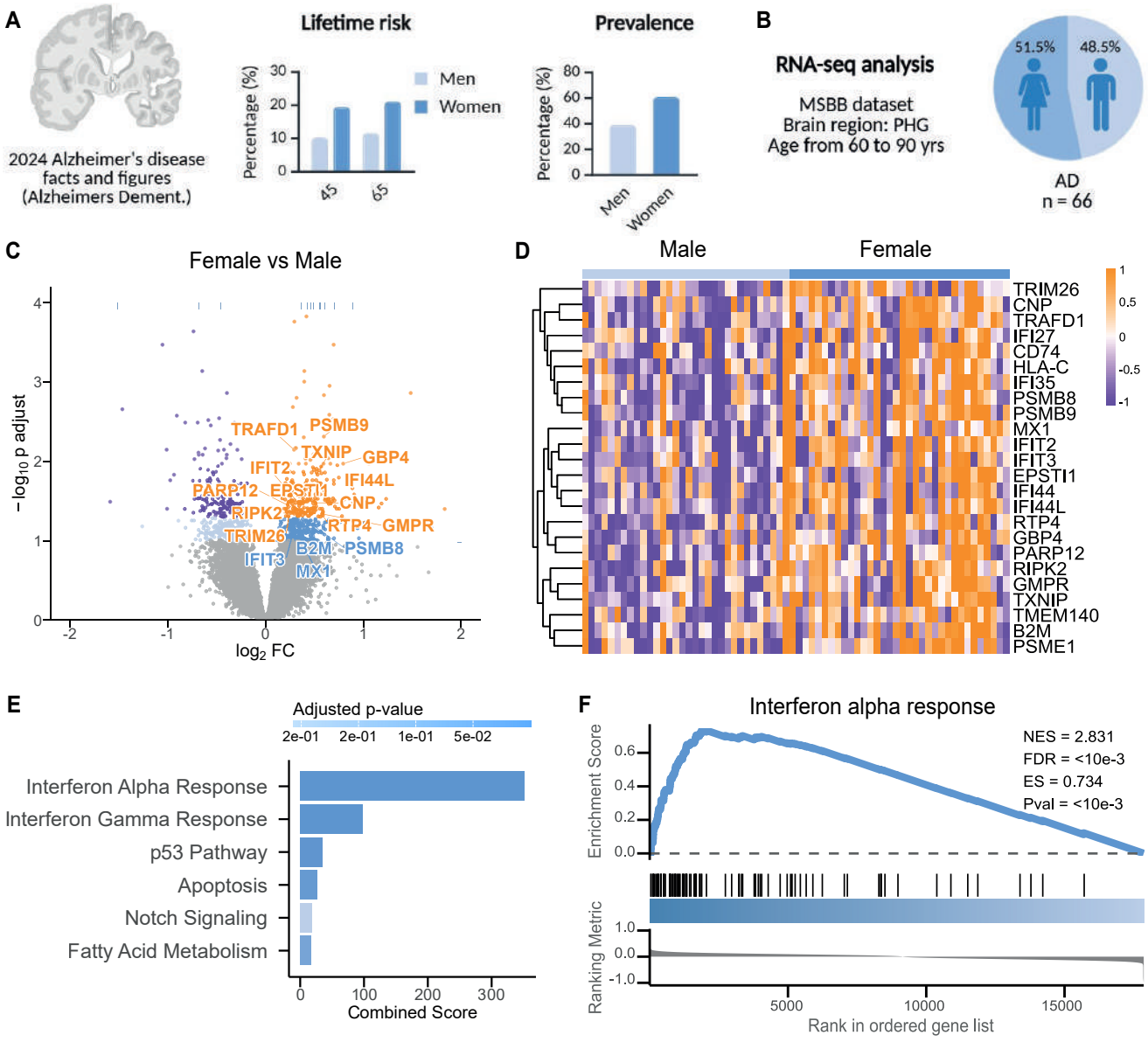
A
2024 Alzheimer's disease facts and figures (Alzheimers Dement.)
Lifetime risk
Percentage (%)
Men
Women
45
65
Prevalence
Men
Women
B
RNA-seq analysis
MSBB dataset
Brain region: PHG
Age from 60 to 90 yrs
51.5%
48.5%
AD
n = 66
C
Female vs Male
$-\log_{10}$ p adjust
$\log_2$ FC
TRAFD1
PSMB9
TXNIP
GBP4
IFIT2
IFI44L
PARP12
EPSTI1
CNP
RIPK2
RTP4
GMPR
TRIM26
B2M
PSMB8
IFIT3
MX1
D
Male
Female
TRIM26
CNP
TRAFD1
IFI27
CD74
HLA-C
IFI35
PSMB8
PSMB9
MX1
IFIT2
IFIT3
EPSTI1
IFI44
IFI44L
RTP4
GBP4
PARP12
RIPK2
GMPR
TXNIP
TMEM140
B2M
PSME1
E
Adjusted p-value
2e-01
2e-01
1e-01
5e-02
Interferon Alpha Response
Interferon Gamma Response
p53 Pathway
Apoptosis
Notch Signaling
Fatty Acid Metabolism
Combined Score
F
Interferon alpha response
Enrichment Score
NES = 2.831
FDR = <10e-3
ES = 0.734
Pval = <10e-3
Ranking Metric
Rank in ordered gene list

**Figure 1**

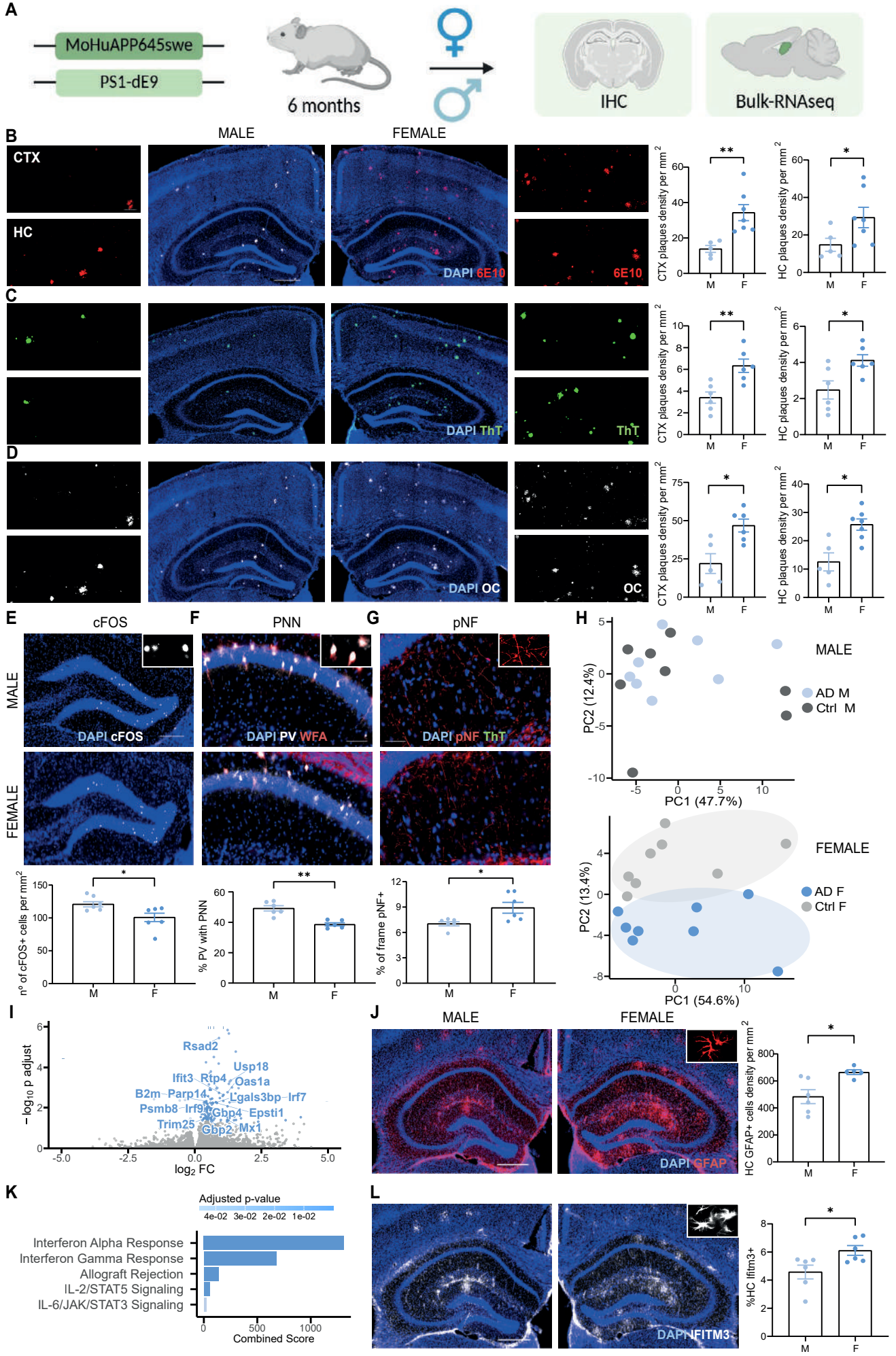
A
MoHuAPP645swe
PS1-dE9
6 months
IHC
Bulk-RNAseq
B
MALE
FEMALE
CTX
HC
DAPI 6E10
6E10
CTX plaques density per mm2
HC plaques density per mm2
C
DAPI ThT
ThT
D
DAPI OC
OC
E
cFOS
F
PNN
G
pNF
MALE
FEMALE
DAPI cFOS
DAPI PV WFA
DAPI pNF ThT
n° of cFOS+ cells per mm2
% PV with PNN
% of frame pNF+
H
MALE
AD M
Ctrl M
PC2 (12.4%)
PC1 (47.7%)
FEMALE
AD F
Ctrl F
PC2 (13.4%)
PC1 (54.6%)
I
Rsad2
Usp18
Ifit3
Rtp4
Oas1a
B2m
Parp14
Lgals3bp
Irf7
Psmb8
Irf9
Gbp4
Epsti1
Trim25
Gbp2
Mx1
– log10 p adjust
log2 FC
J
MALE
FEMALE
DAPI GFAP
HC GFAP+ cells density per mm2
K
Adjusted p-value
4e-02 3e-02 2e-02 1e-02
Interferon Alpha Response
Interferon Gamma Response
Allograft Rejection
IL-2/STAT5 Signaling
IL-6/JAK/STAT3 Signaling
Combined Score
L
DAPI IFITM3
%HC Ifitm3+

**Figure 2**

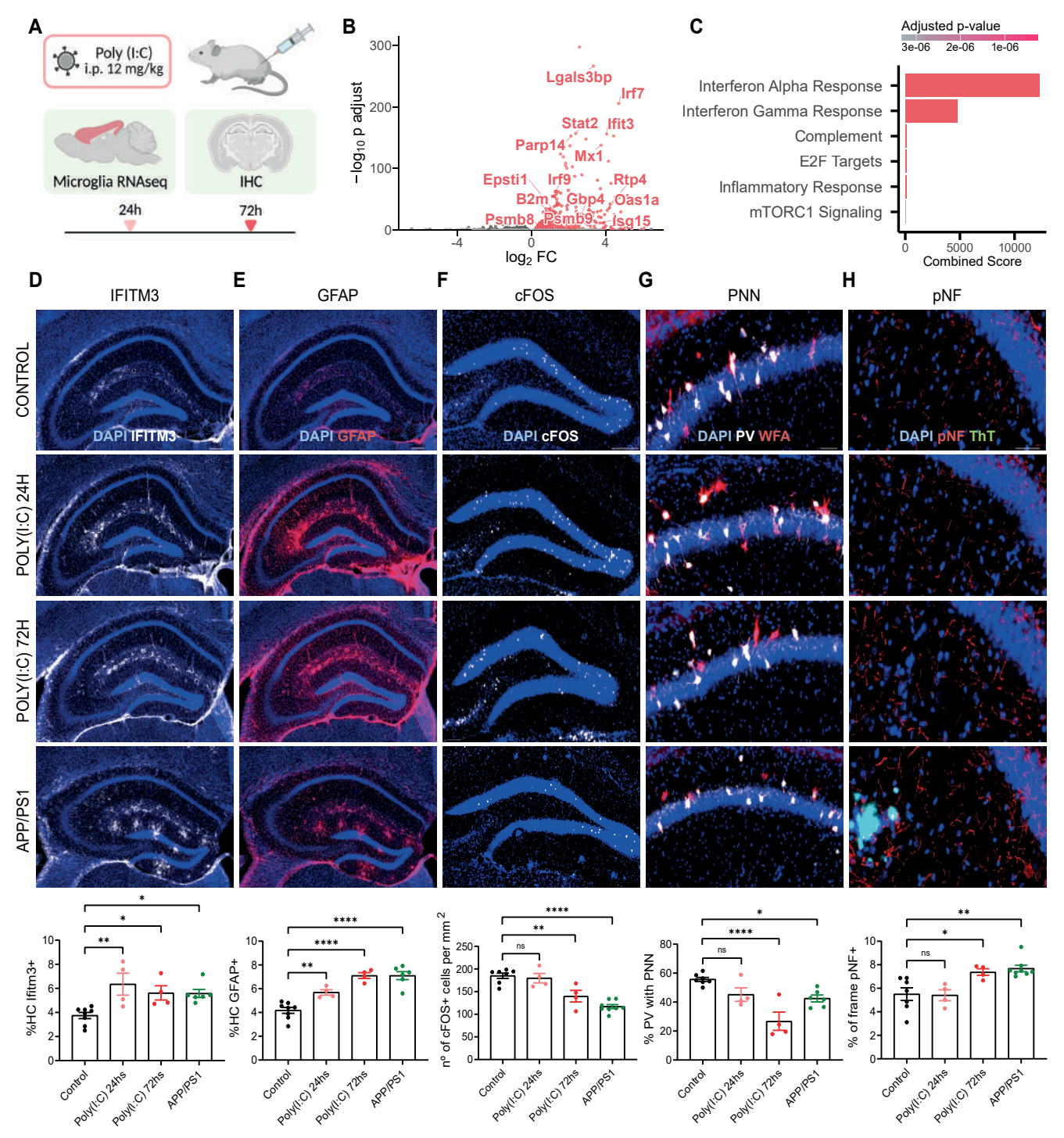
A
Poly (I:C)
i.p. 12 mg/kg
Microglia RNAseq
IHC
24h
72h
B
−log10 p adjust
log2 FC
Lgals3bp
Irf7
Stat2
Ifit3
Parp14
Mx1
Epsti1
Irf9
Rtp4
B2m
Gbp4
Oas1a
Psmb8
Psmb9
Isg15
C
Adjusted p-value
3e-06
2e-06
1e-06
Interferon Alpha Response
Interferon Gamma Response
Complement
E2F Targets
Inflammatory Response
mTORC1 Signaling
Combined Score
D
IFITM3
E
GFAP
F
cFOS
G
PNN
H
pNF
CONTROL
POLY(I:C) 24H
POLY(I:C) 72H
APP/PS1
DAPI IFITM3
DAPI GFAP
DAPI cFOS
DAPI PV WFA
DAPI pNF ThT
%HC Ifitm3+
%HC GFAP+
nº of cFOS+ cells per mm 2
% PV with PNN
% of frame pNF+
Control
Poly(I:C) 24hs
Poly(I:C) 72hs
APP/PS1
ns

**Figure 3**

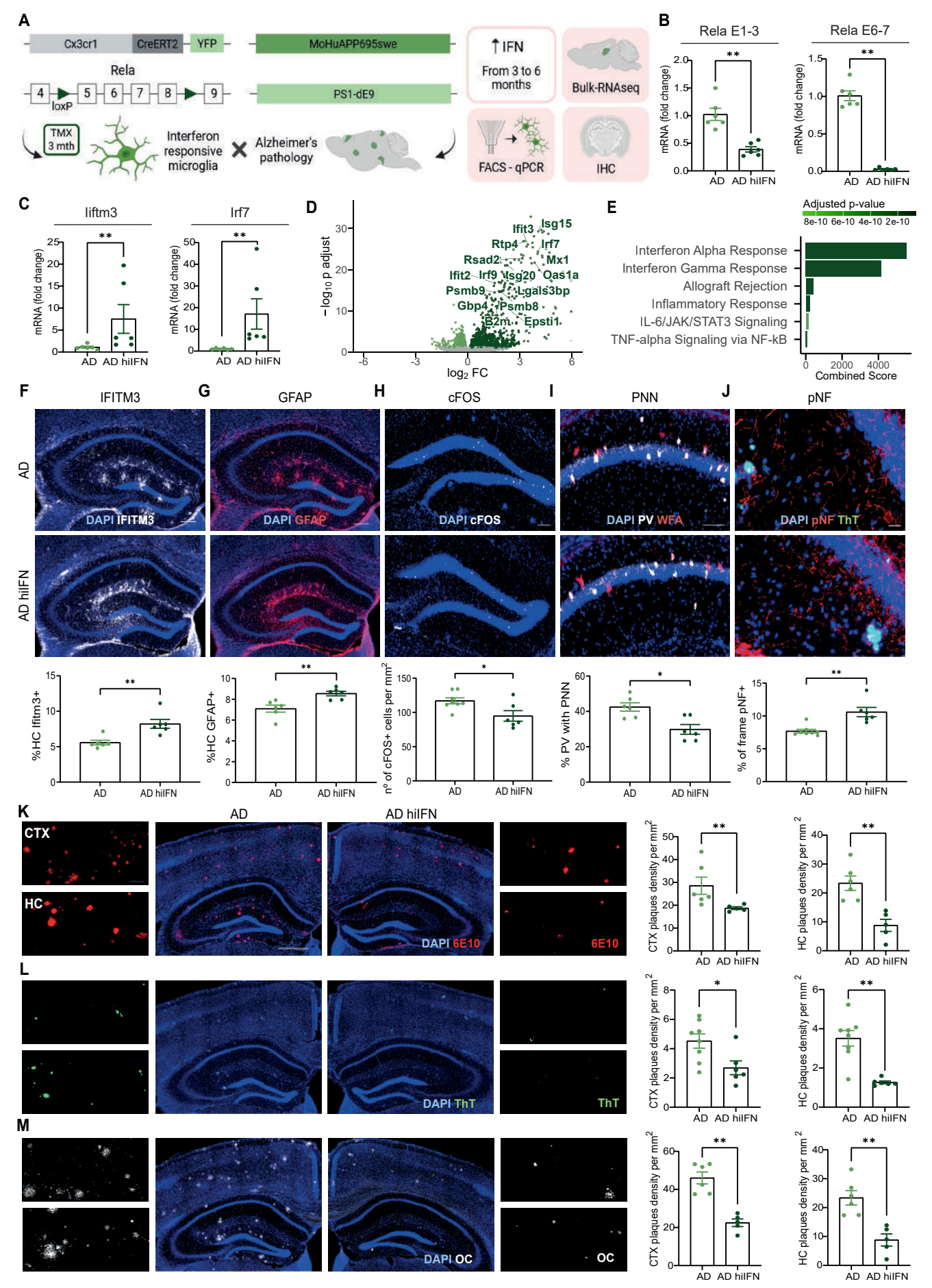
A
Cx3cr1
CreERT2
YFP
MoHuAPP695swe
Rela
loxP
PS1-dE9
TMX 3 mth
Interferon responsive microglia
Alzheimer's pathology
IFN
From 3 to 6 months
Bulk-RNAseq
FACS - qPCR
IHC
B
Rela E1-3
Rela E6-7
mRNA (fold change)
AD
AD hiIFN
C
Iiftm3
Irf7
D
−log10 p adjust
log2 FC
Ifit3
Isg15
Rtp4
Irf7
Rsad2
Mx1
Ifit2
Irf9
Isg20
Oas1a
Psmb9
Lgals3bp
Gbp4
Psmb8
B2m
Epsti1
E
Adjusted p-value
Interferon Alpha Response
Interferon Gamma Response
Allograft Rejection
Inflammatory Response
IL-6/JAK/STAT3 Signaling
TNF-alpha Signaling via NF-kB
Combined Score
F
IFITM3
G
GFAP
H
cFOS
I
PNN
J
pNF
DAPI IFITM3
DAPI GFAP
DAPI cFOS
DAPI PV WFA
DAPI pNF ThT
%HC Ifitm3+
%HC GFAP+
nº of cFOS+ cells per mm2
% PV with PNN
% of frame pNF+
K
CTX
HC
DAPI 6E10
6E10
CTX plaques density per mm2
HC plaques density per mm2
L
DAPI ThT
ThT
M
DAPI OC
OC

**Figure 4**

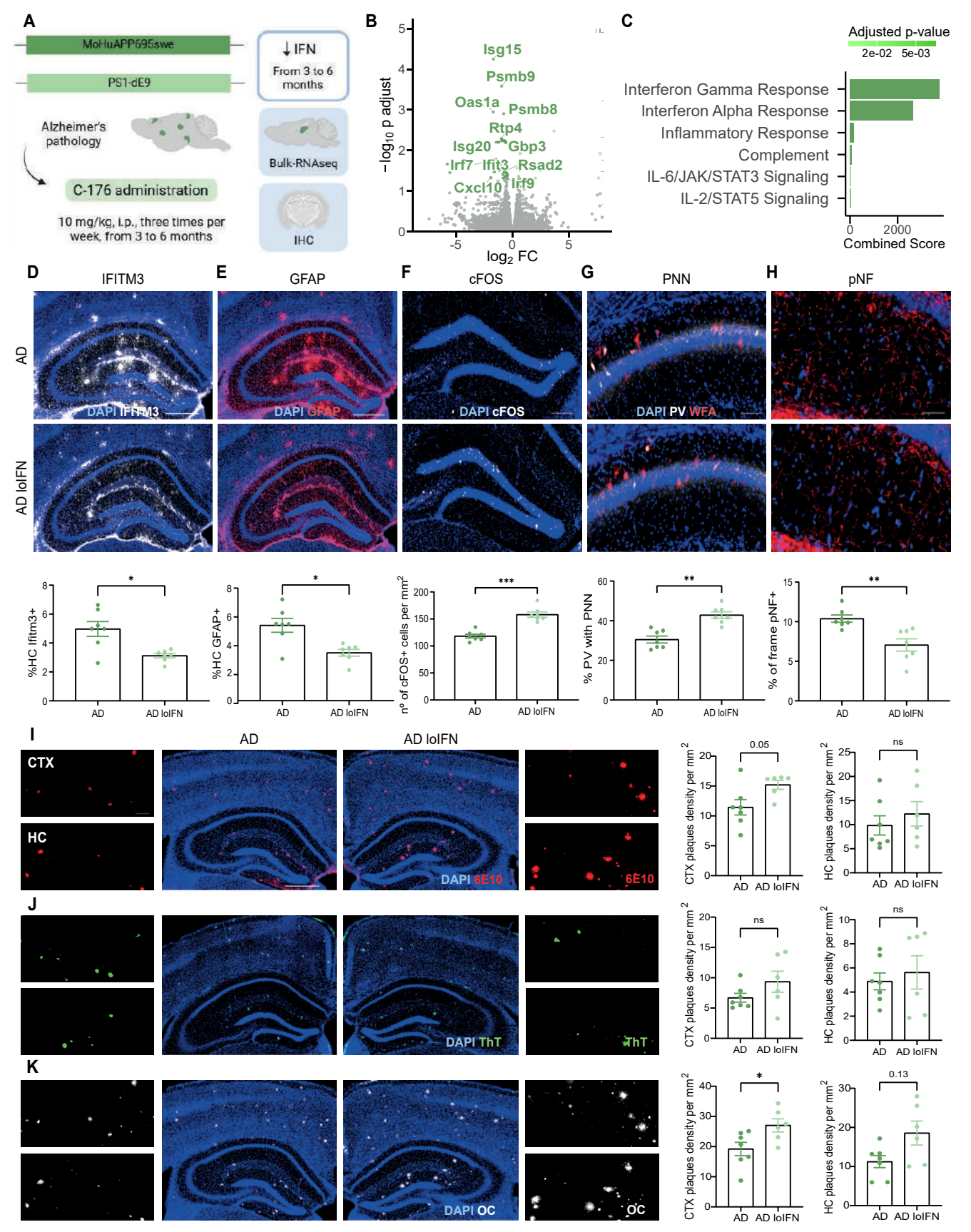
A
MoHuAPP695swe
PS1-dE9
Alzheimer's pathology
C-176 administration
10 mg/kg, i.p., three times per week, from 3 to 6 months
↓IFN
From 3 to 6 months
Bulk-RNAseq
IHC
B
Isg15
Psmb9
Oas1a
Psmb8
Rtp4
Isg20
Gbp3
Irf7
Ifit3
Rsad2
Cxcl10
Irf9
−log10 p adjust
log2 FC
C
Adjusted p-value
2e-02
5e-03
Interferon Gamma Response
Interferon Alpha Response
Inflammatory Response
Complement
IL-6/JAK/STAT3 Signaling
IL-2/STAT5 Signaling
Combined Score
D
IFITM3
E
GFAP
F
cFOS
G
PNN
H
pNF
AD
AD IoIFN
DAPI IFITM3
DAPI GFAP
DAPI cFOS
DAPI PV WFA
%HC Ifitm3+
%HC GFAP+
nº of cFOS+ cells per mm2
% PV with PNN
% of frame pNF+
I
CTX
HC
DAPI 6E10
6E10
CTX plaques density per mm2
HC plaques density per mm2
J
DAPI ThT
ThT
K
DAPI OC
OC
ns

**Figure 5**

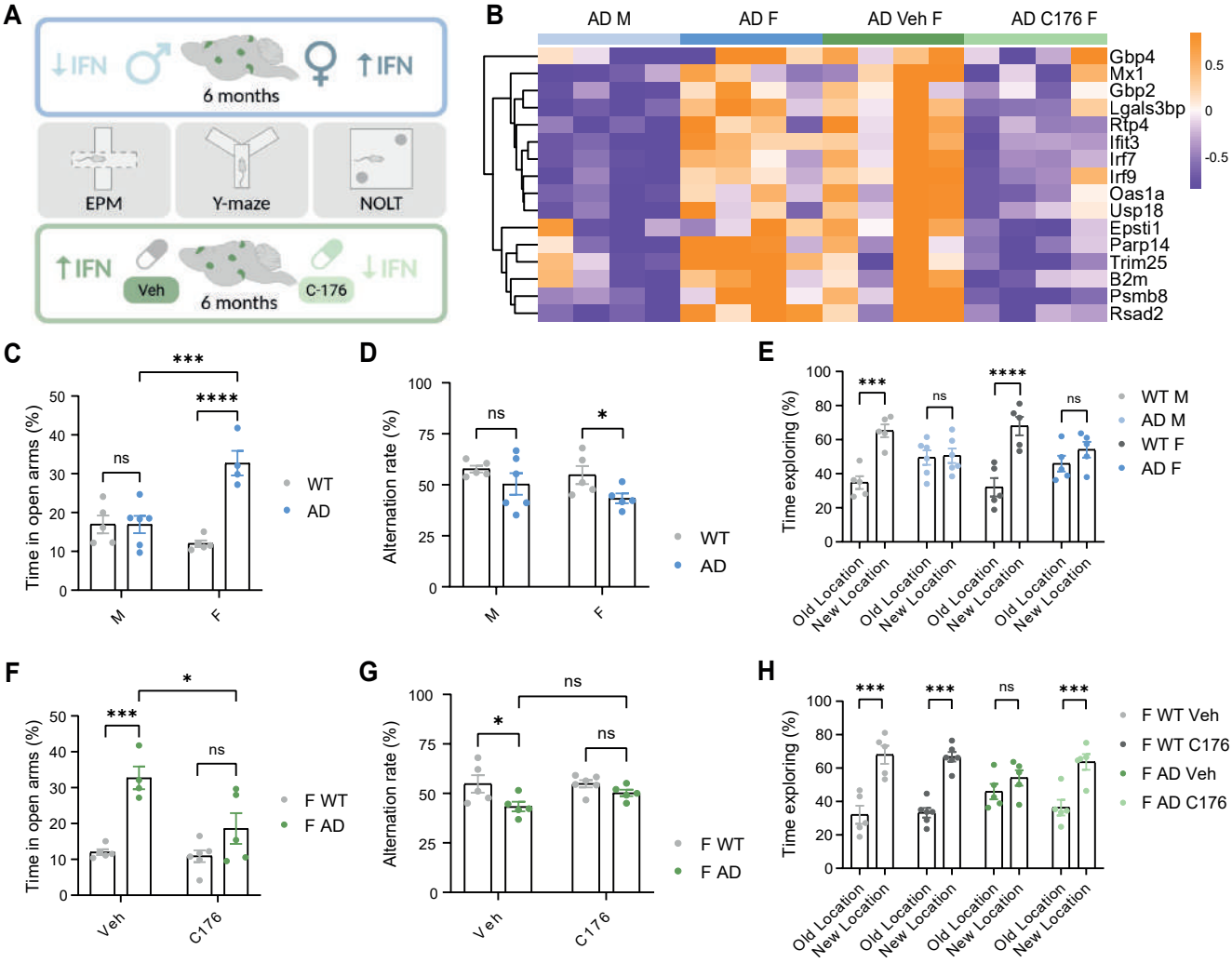
A
↓IFN
↑IFN
6 months
EPM
Y-maze
NOLT
↑IFN
Veh
6 months
C-176
↓IFN
B
AD M
AD F
AD Veh F
AD C176 F
Gbp4
Mx1
Gbp2
Lgals3bp
Rtp4
Ifit3
Irf7
Irf9
Oas1a
Usp18
Epsti1
Parp14
Trim25
B2m
Psmb8
Rsad2
0.5
0
-0.5
C
Time in open arms (%)
ns
***
****
M
F
WT
AD
D
Alternation rate (%)
ns
*
M
F
WT
AD
E
Time exploring (%)
***
ns
****
ns
Old Location
New Location
WT M
AD M
WT F
AD F
F
Time in open arms (%)
***
*
ns
Veh
C176
F WT
F AD
G
Alternation rate (%)
*
ns
ns
Veh
C176
F WT
F AD
H
Time exploring (%)
***
***
ns
***
Old Location
New Location
F WT Veh
F WT C176
F AD Veh
F AD C176

**Figure 6**

# Supplementary figures

**Extended Data Fig. 1. Increased interferon signaling in Alzheimer's disease is sex-specific and absent in controls.** (A) PCA of AD PHG RNA-seq data from the MSBB cohort (including samples from individuals aged 60–90 at death), with one misannotated male sample (excluded from analyses) clustering with female samples. (B) Heatmap of canonical sex chromosome gene expression in PHG from AD patients aged 60 to 90 years, confirming accurate sex annotation except for the misannotated male sample (bold). n = 32 (male AD), 34 (female AD). (C–E) Functional enrichment of differentially expressed genes (FDR < 0.05) in PHG tissue of AD patients (60 to 90 years). (C) Upregulated pathways in AD versus age-matched control samples. (D) Upregulated pathways in male AD versus age-matched male controls. (E) Upregulated pathways in female AD versus age-matched female controls. Female AD samples exhibit stronger interferon signatures, whereas in male AD samples the enrichment of epithelial–mesenchymal transition and inflammatory response pathways are prominent. (F) Volcano plot of differential gene expression in PHG of control individuals (female vs. male, aged from 60 to 90 years), showing no significant changes in interferon-related genes in females (gray, non-significant). n = 23 (male AD), 19 (female AD). (G) Functional enrichment analysis of differentially expressed genes (FDR < 0.05) in the PHG from control individuals (female vs. male, aged from 60 to 90 years), showing no significant activation of interferon alpha or gamma response pathways. n = 23 (male AD), 19 (female AD). (H) GSEA plot of the interferon alpha response pathway in control individuals (female vs. male, aged from 60 to 90 years). n = 23 (male AD), 19 (female AD).

**Extended Data Fig. 2. Sex-dependent neuropathological and transcriptomic changes in APP/PS1 Mice.** (A) Quantification of Aβ plaque size by 6E10 immunohistochemistry in the cortex (CTX) and hippocampus (HC) of 6-month-old male and female APP/PS1 mice, showing no significant differences in plaque size between sexes (ns, $P > 0.05$, Mann-Whitney test). (B) Quantification of fibrillar Aβ deposit size by Thioflavin T staining in CTX and HC, confirming no significant differences in deposit size between sexes (ns, $P > 0.05$, Mann-Whitney test). (C) Quantification of β-sheet-rich Aβ conformation size by OC antibody staining in CTX and HC, showing no significant differences between sexes (ns, $P > 0.05$, Mann-Whitney test). (D) Quantification of WFA-positive structure number in CA1, showing no significant differences between (ns, $P > 0.05$, Mann-Whitney test). (E) Volcano plot of differential gene expression in HC contrasting APP/PS1 vs control, highlighting top 15 significant genes (green, $P < 0.05$ in APP/PS1; dark grey, $P < 0.05$ in control; gray, non-significant). (F) Functional enrichment analysis from HC tissue of mice showing enriched pathways for APP/PS1 mice contrasted against control mice, where no interferon pathway was highlighted. (G) Quantification of GFAP immunohistochemistry density in the cortex, showing increased astrogliosis in female APP/PS1 mice (**$P \leq 0.01$), Mann-Whitney test). (H) GSEA plot of the interferon alpha response pathway in the hippocampi of female vs. male APP/PS1 mice. (I) Quantification of IFITM3 immunohistochemistry intensity in the cortex,

showing increased labeling in female APP/PS1 (**$P \leq 0.01$), Mann-Whitney test). Data from 6-month-old APP/PS1 mice. IHC: n = 7 (control), 4 (Poly(I:C) 24h), 4 (Poly(I:C) 72h), and 6 (APP/PS1). IHC: n = 12 (6 females, 6 males). RNA-seq: n = 8 AD females, 8 AD males, 8 WT females, 8 WT males. Data represent mean ± SEM.

**Extended Data Fig. 3. Poly(I:C)-induced interferon signaling and neuropathological changes in wild-type mice.** (A) PCA of hippocampal RNA-seq data from 3-month-old wild-type C57BL/6 mice treated with poly(I:C) (12 mg/kg) and analyzed at 24 hours, compared to untreated controls, showing transcriptomic divergence among the two groups. (B) GSEA plot of the interferon alpha response pathway in the HC of poly(I:C)-treated mice (24 hours) vs. untreated controls, confirming significant enrichment of interferon alpha signaling. (C) Quantification of IFITM3 immunohistochemistry intensity in the cortex, showing increased labeling in poly(I:C)-treated mice at 24 hours (****$P < 0.0001$), and 72 hours (*$P < 0.05$), and in APP/PS1 mice (*$P < 0.05$) compared to controls (Mann-Whitney test). (D) Quantification of GFAP immunohistochemistry intensity in the cortex, indicating no significant changes in astrogliosis in poly(I:C)-treated mice at 24 hours (ns, $P > 0.05$) and 72 hours (ns, $P > 0.05$), and an increased in APP/PS1 mice (****$P < 0.0001$) compared to controls (Mann-Whitney test). (E) Quantification of WFA-positive structure number in CA1, showing no significant changes in poly(I:C)-treated mice at 24 hours (ns, $P > 0.05$), and fewer structures at 72 hours (**$P < 0.01$) and APP/PS1 mice (*$P < 0.05$) compared to controls (Mann-Whitney test). Data from 3-month-old wild-type C57BL/6 mice (RNA-seq at 24 hours, immunohistochemistry at 24 and 72 hours) and 6-month-old APP/PS1 mice. IHC: n = 7 (control), 4 (Poly(I:C) 24h), 4 (Poly(I:C) 72h), and 6 (APP/PS1). Poly(I:C) groups included only males; other groups were sex-balanced (3 females, 3 males for APP/PS1; 3 females, 4 males for controls). RNA-seq: n = 4 (control), 3 (Poly(I:C) 24h). Data represent mean ± SEM.

**Extended Data Fig. 4. Neuropathological and transcriptomic effects of enhanced interferon signaling in APP/PS1 mice.** (A) PCA of hippocampal RNA-seq data from 6-month-old APP/PS1 (AD) and microglia-specific *Rela* knockout (AD hiIFN) mice, showing transcriptomic divergence between the two groups. (B) GSEA plot of the interferon alpha response pathway in the hippocampus of AD hiIFN vs. AD mice, confirming significant enrichment of interferon alpha signaling. (C) Heatmap of interferon-alpha-related gene expression in hippocampal tissue from male and female AD and AD hiIFN mice, not highlighting a sex-biased transcriptomic profile. (D) Quantification of IFITM3 immunohistochemistry intensity in the cortex, showing higher labeling in AD hiIFN vs. AD mice (**$P < 0.01$, Mann-Whitney test). (E) Quantification of GFAP immunohistochemistry intensity in the cortex, indicating nearly significant increase in astrogliosis in AD hiIFN vs. AD mice ($P = 0.06$, Mann-Whitney test). (F) Quantification of 6E10 immunohistochemistry for Aβ plaque size in the cortex (CTX) and hippocampus (HC), showing reduced plaque size in AD hiIFN vs. AD mice hippocampus (*$P < 0.05$) and no significant changes in cortex (ns, $P > 0.05$) (Mann-Whitney test). (G) Quantification of Thioflavin T staining for fibrillar Aβ deposit size in CTX (ns, $P > 0.05$) and HC (ns, $P > 0.05$), showing no significant changes in AD hiIFN

vs. AD mice (Mann-Whitney test). (H) Quantification of OC staining for β-sheet-rich Aβ conformation size in CTX (ns, $P > 0.05$) and HC (ns, $P > 0.05$), showing no significant changes in AD hiIFN vs. AD mice (Mann-Whitney test). Data from 6-month-old AD hiIFN and APP/PS1 mice. IHC: n = 6 per group (3 females, 3 males). RNA-seq: n = 8 per group (4 females, 4 males). Data represent mean ± SEM.

**Extended Data Fig. 5. Effects of STING inhibition on BV2 microglial cells and neuropathology in APP/PS1 mice.** (A) Expression of interferon-stimulated genes (*Irf7*, *Ifitm3*, *Stat2*) and the anti-inflammatory cytokine *Il10* in BV2 microglial cells treated with vehicle (Veh) or STING inhibitor C-176, with or without poly(I:C) stimulation (ns, $P > 0.05$, $^{**}P < 0.01$, $^{***}P < 0.001$, $^{****}P < 0.0001$, Mann-Whitney test). (B) Heatmap of interferon-alpha-related gene expression in hippocampal tissue from male and female 6-month-old APP/PS1 (AD) and C-176-treated APP/PS1 (AD loIFN) mice, highlighting a higher transcriptomic profile switch in females. (C) GSEA plot of the interferon alpha response pathway from HC tissue of treated vs. untreated female AD mice, confirming reduced enrichment of interferon signaling in treated females. (D) Volcano plot of differential gene expression in the hippocampus of male AD loIFN vs. untreated AD mice, showing no significant changes in interferon-related genes (gray, non-significant). (E) Functional enrichment analysis from HC tissueof male AD loIFN vs. untreated AD mice, showing no significant reduction of the interferon alpha or gamma response pathways. (F) Quantification of IFITM3 immunohistochemistry intensity in the cortex, showing lower labeling in untreated AD mice vs. AD loIFN ($^{*}P < 0.05$, Mann-Whitney test). (G) Quantification of GFAP immunohistochemistry intensity in the cortex, indicating nearly significance decrease of astrogliosis in AD loIFN vs. untreated AD mice ($P = 0{,}09$, Mann-Whitney test). (H) Quantification of WFA-positive structure number in CA1, showing an increase in AD loIFN vs. untreated AD mice ($^{*}P > 0.05$, Mann-Whitney test). (I) Quantification of 6E10 immunohistochemistry for Aβ plaque size in the cortex (CTX) and hippocampus (HC), showing no significant changes in AD loIFN vs. untreated AD mice (ns, $P > 0.05$, Mann-Whitney test). (J) Quantification of Thioflavin T staining for fibrillar Aβ deposit size in CTX and HC, showing no significant changes in AD loIFN vs. untreated AD mice (ns, $P > 0.05$, Mann-Whitney test). (K) Quantification of OC staining for β-sheet-rich Aβ conformation size in CTX ($P > 0.05$) and HC (ns, $P > 0.05$), showing no significant changes in plaques size in AD loIFN vs. untreated AD mice (Mann-Whitney test). Data from BV2 cell cultures and 6-month-old AD loIFN and APP/PS1 mice. qPCR: n = 4 per group. IHC: n = 6 per group (3 females, 3 males). RNA-seq: n = 8 AD (females), 4 AD loIFN (females). Data represent mean ± SEM.

**Extended Data Fig. 6. Behavioral tasks with no significant differences by sex or STING inhibition in APP/PS1 mice.** (A) Percentage of distance traveled in the center zone of the open field test in 6-month-old male and female WT and APP/PS1 (AD) mice, showing reduced center exploration in AD females compared to males and WT controls ($P = 0.05$, two-way ANOVA with Tukey's post hoc test). (B) Percentage of time spent exploring in the T-maze test, showing no significant differences between sexes or genotypes ($^{***}P < 0.001$, $^{****}P < 0.0001$, two-way ANOVA with Tukey's post hoc

test.) (C) Percentage of freezing during the contextual phase of fear conditioning, showing no significant differences across groups (ns, $P > 0.05$, two-way ANOVA with Tukey's post hoc test). (D) Percentage of freezing during the auditory cue in cued fear conditioning, also showing no significant differences (ns, $P > 0.05$, two-way ANOVA with Tukey's post hoc test). (E) Percentage of distance traveled in the center zone of the open field test in female AD mice treated with vehicle or C-176, showing a non-significant trend toward increased center exploration in C-176–treated mice ($P = 0.11$, two-way ANOVA with Tukey's post hoc test). (F) Percentage of time spent exploring in the T-maze test in female AD mice, showing no difference between vehicle- and C-176–treated groups (ns, $P > 0.05$, two-way ANOVA with Tukey's post hoc test). (G) Percentage of freezing during contextual fear conditioning in female AD mice, showing no effect of C-176 treatment (ns, $P > 0.05$, two-way ANOVA with Tukey's post hoc test). (H) Percentage of freezing during cued fear conditioning in female AD mice, showing no effect of C-176 treatment (ns, $P > 0.05$, two-way ANOVA with Tukey's post hoc test). All behavioral tests were performed in 6-month-old APP/PS1 mice. n = 5 (male WT), 6 (male AD), 5 (female WT), 5 (female AD), 5 (female WT + vehicle), 5 (female WT + C-176), 5 (female AD + vehicle), and 5 (female AD + C-176). Data represent mean ± SEM.

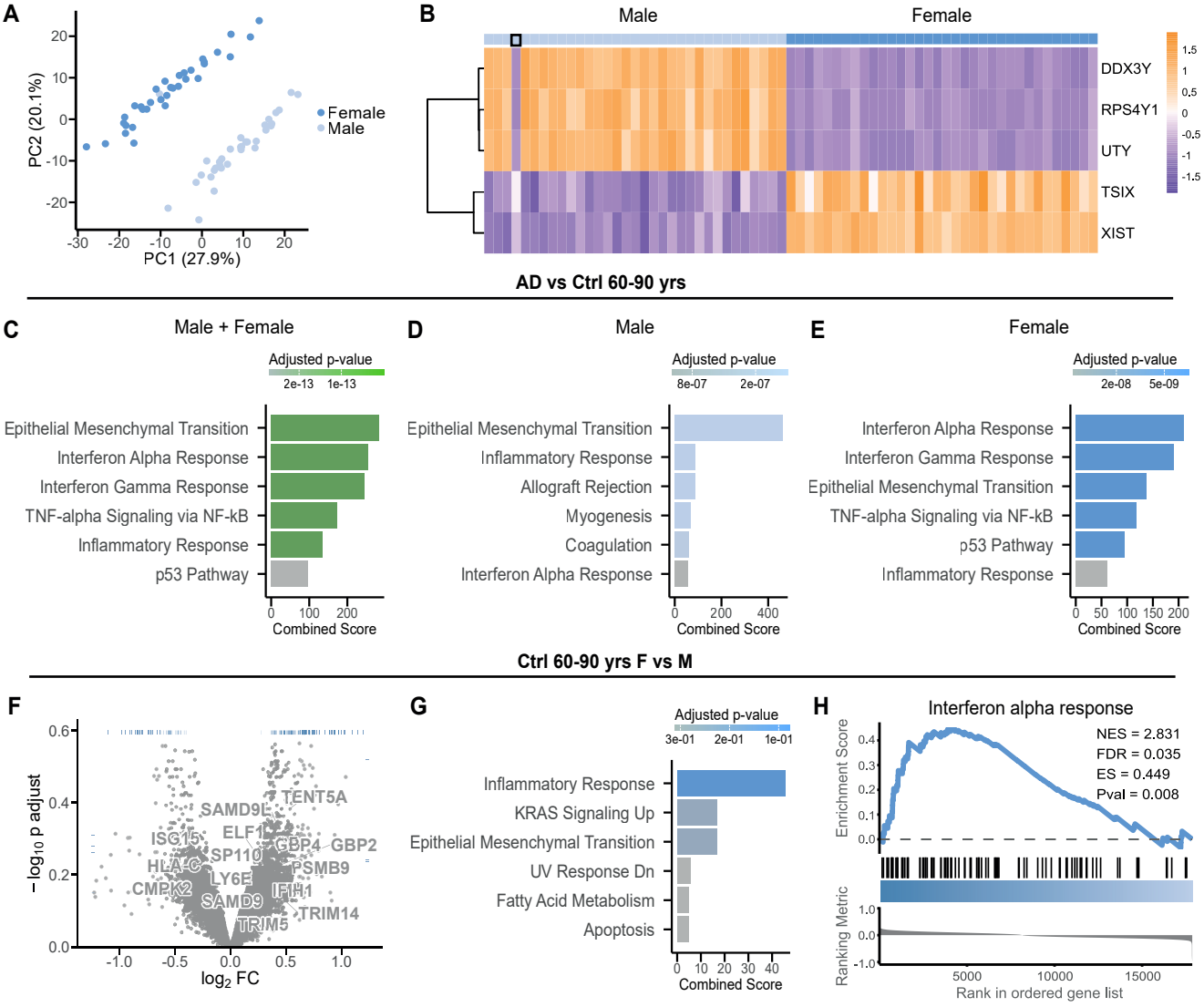


**Supplemental Figure 1**

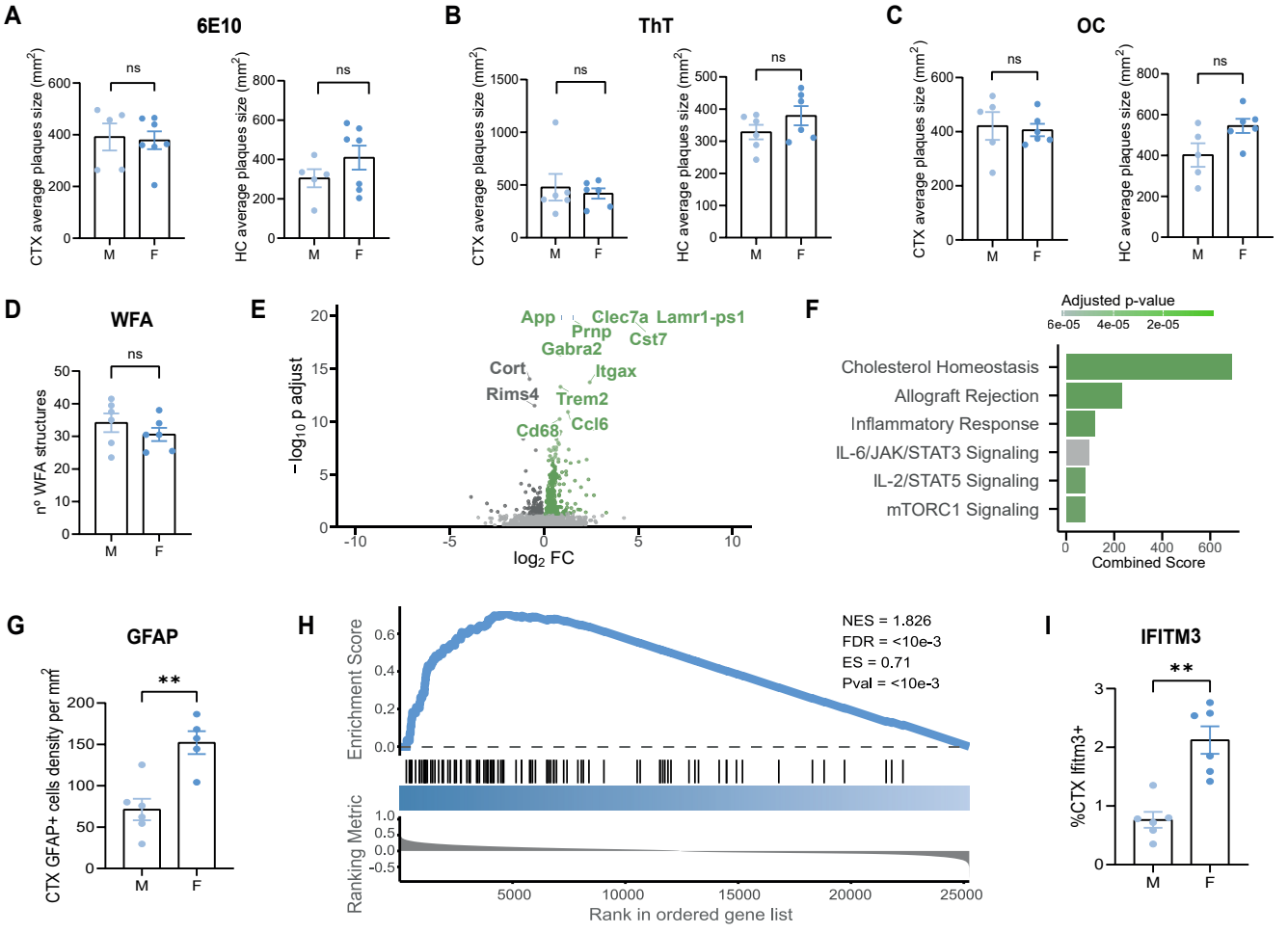


**Supplemental Figure 2**

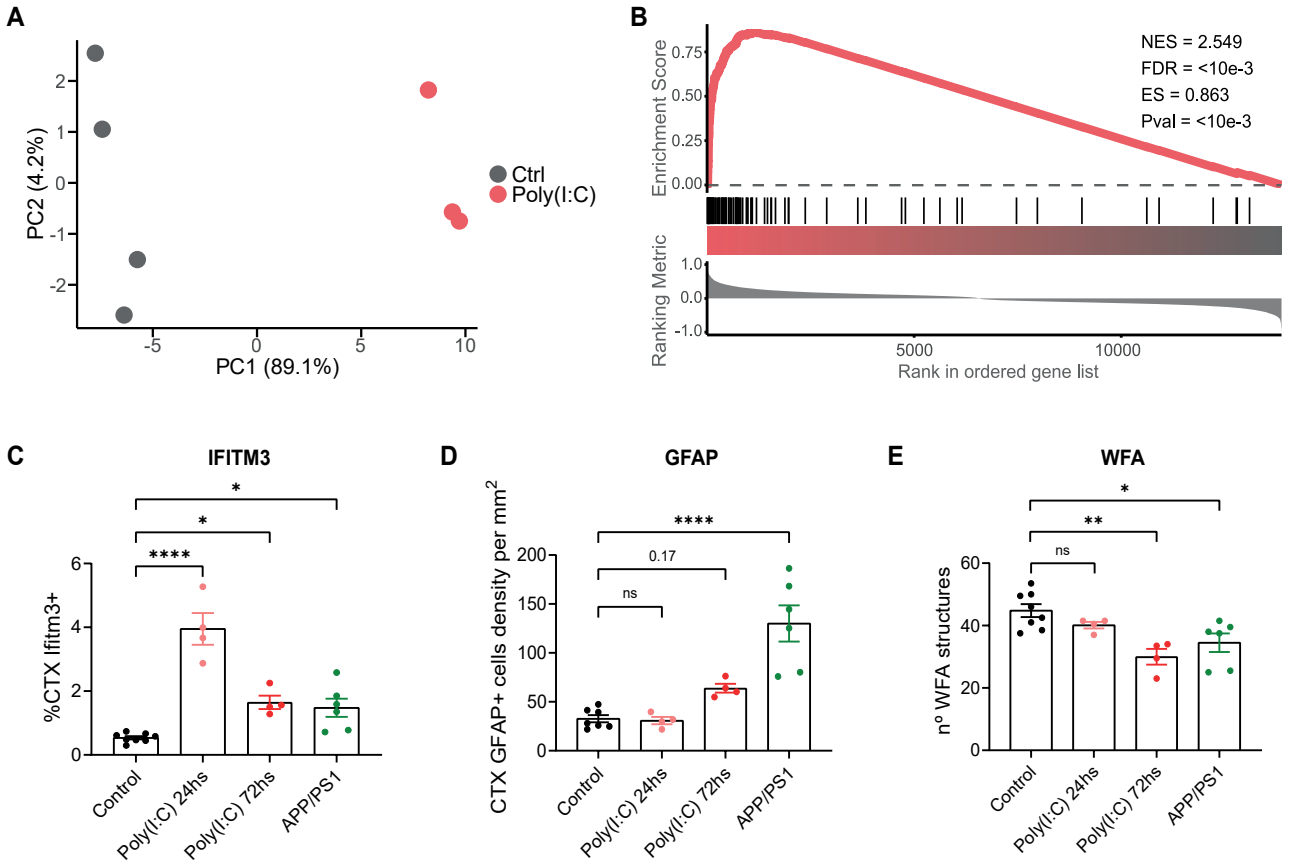


**Supplemental Figure 3**

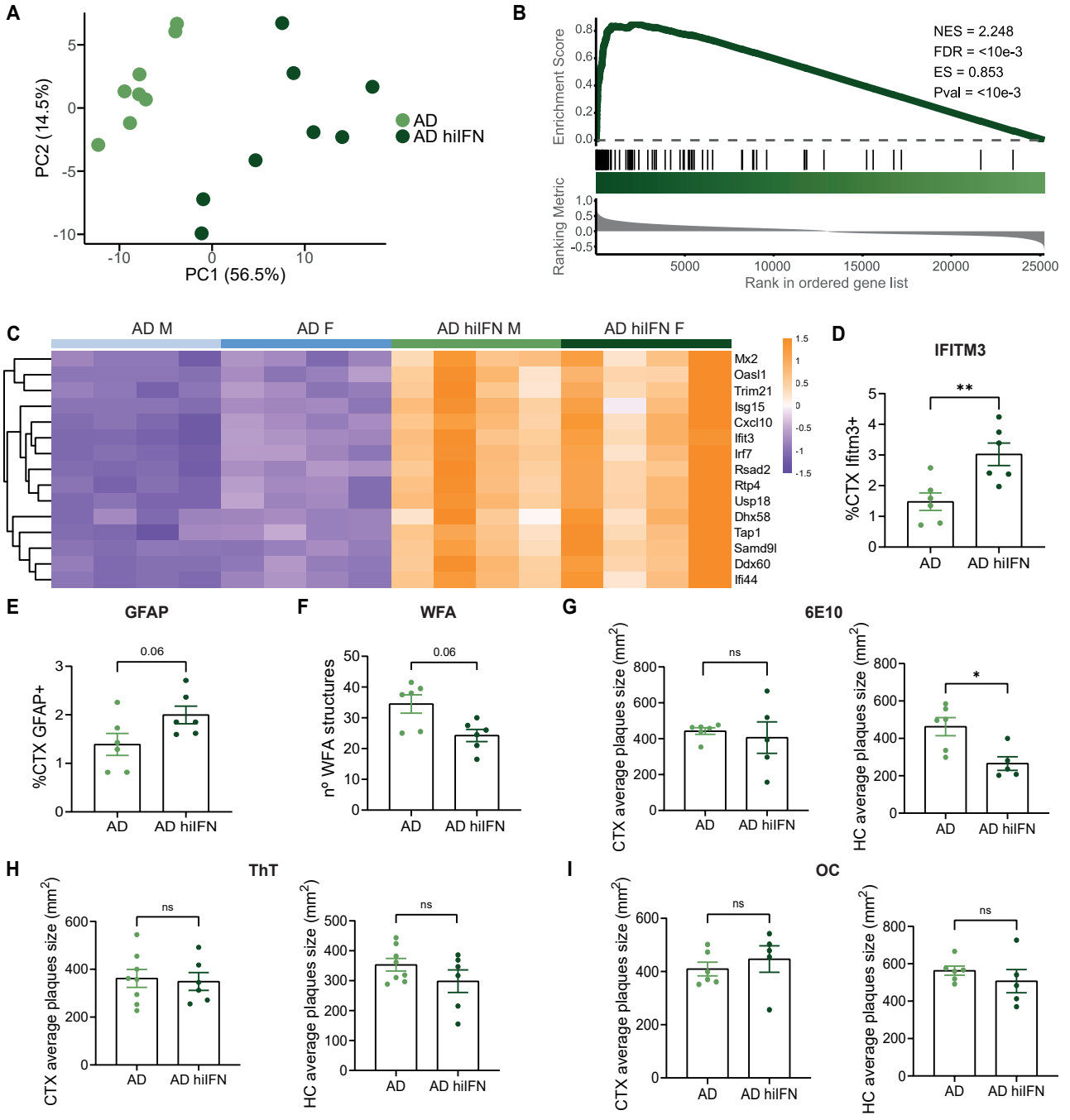


**Supplemental Figure 4**

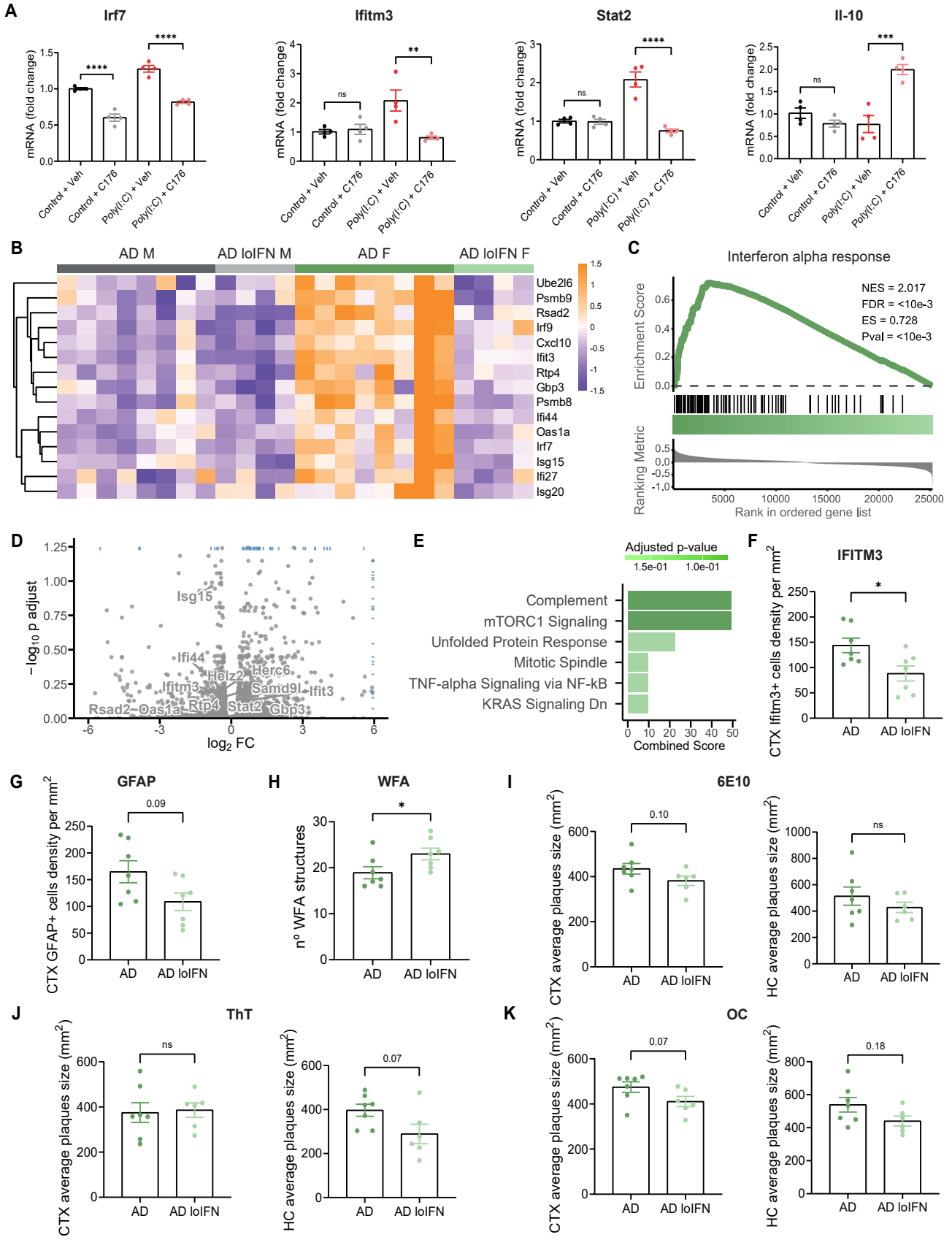


**Supplemental Figure 5**

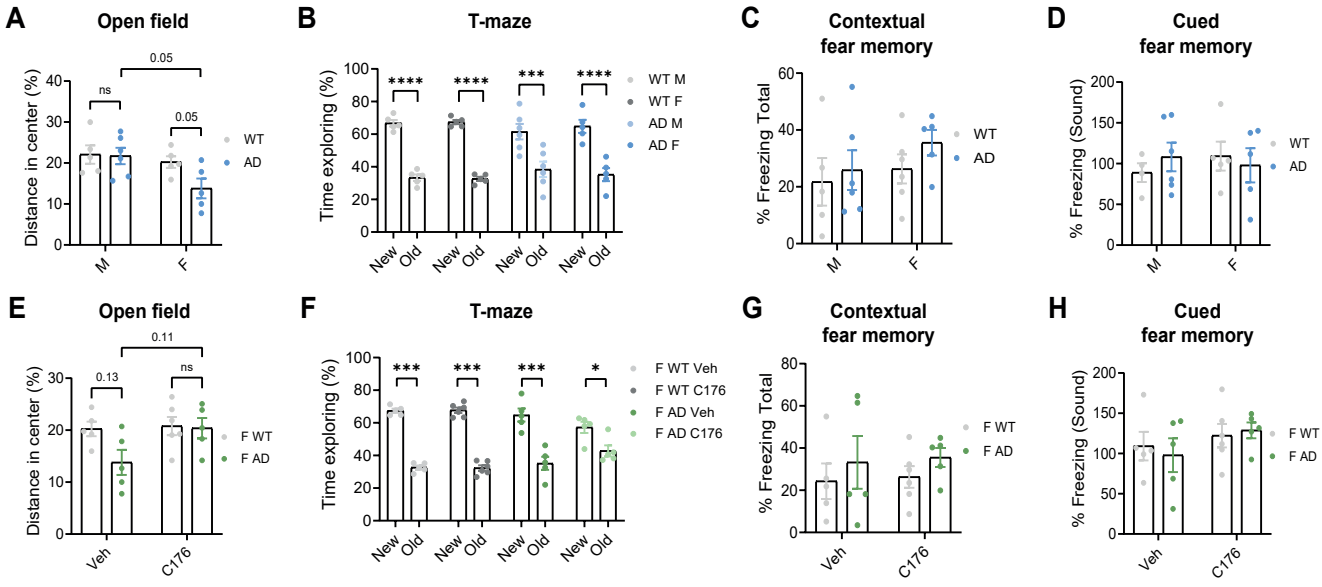


**Supplemental Figure 6**